

1
2
3
4
5
6
7
8
9
10
11
12
13
14
15
16

New particle formation in the Svalbard region 2006 - 2015

Jost Heintzenberg¹, Peter Tunved², Martí Galí³, and Caroline Leck⁴

- 1: Leibniz Institute for Tropospheric Research (TROPOS), Permoserstr. 15, 04318 Leipzig, Germany
- 2: Department of Environmental Science and Analytical Chemistry (ACES), Stockholm University, 10691 Stockholm, Sweden
- 3: Takuvik Joint International Laboratory & Québec-Océan, Université Laval, G1V 0A6 Québec, Canada
- 4: Department of Meteorology, Stockholm University (MISU), 10691 Stockholm, Sweden

17 Abstract

18

19 Events of new particle formation, (NPF), were analyzed in a ten-year data set of hourly
20 particle size distributions recorded on Mt. Zeppelin, Spitsbergen, Svalbard. Three different
21 types of NPF-events were identified through objective search algorithms. The first and
22 simplest algorithm utilizes short-term increases in particle concentrations below 25 nm,
23 (PCT-events). The second one builds on the growth of the sub-50 nm diameter-median,
24 (DGR-events), and is most closely related to the classical “banana-type” of events. The third
25 and most complex, so-called multiple-size approach to identifying NPF-events builds on a
26 hypothesis suggesting the concurrent production of polymer gel particles at several sizes
27 below about 60 nm, (MEV-events).

28 As a first and general conclusion we can state that NPF-events are a summer phenomenon
29 and not related to Arctic haze, which is a late winter-to-early spring feature. The occurrence
30 of NPF-events appears to be somewhat sensitive to the available data on precipitation. The
31 seasonal distribution of solar flux suggests some photochemical control that may affect
32 marine biological processes generating particle precursors and/or atmospheric photochemical
33 processes that generate condensable vapors from precursor gases. Notable, the seasonal
34 distribution of the biogenic methanesulfonate, (MSA), follows that of the solar flux although
35 it peaks before the maxima in NPF-occurrence.

36 A host of ancillary data and findings point to varying and rather complex marine biological
37 source processes. The potential source regions for all types of new particle formation appear
38 to be restricted to the marginal ice and open water areas between Northeastern Greenland and
39 Eastern Svalbard. Depending on conditions yet to be clarified new particle formation may
40 become visible as short bursts of particles around 20 nm, (PCT-events), longer events
41 involving condensation growth, (DGR-events), or extended events with elevated
42 concentrations of particles at several sizes below 100 nm, (MEV-events). The seasonal

43 distribution of NPF-events peaks later than that of MSA and, DGR and in particular of MEV-
44 events reach into late summer and early fall with much open, warm, and biologically active
45 waters around Svalbard. Consequently, a simple model to describe the seasonal distribution
46 of the total number of NPF-events can be based on solar flux, and sea surface temperature,
47 representing environmental conditions for marine biological activity, and condensation sink,
48 controlling the balance between new particle nucleation and their condensational growth.
49 Based on the sparse knowledge about the seasonal cycle of gel-forming marine
50 microorganisms and their controlling factors we hypothesize that the seasonal distribution of
51 DGR and more so MEV-events reflect the seasonal cycle of the gel-forming phytoplankton.

52

53

54 **1. Introduction**

55

56 In the late 1970ies and early 1980ies the interest in the Arctic atmospheric aerosol widened
57 from the well-identified winter phenomenon of Arctic haze (Rahn and Shaw, 1977;
58 Heintzenberg and Leck, 1994) to summer conditions in this northernmost remote region. In
59 the pristine Arctic summer air the so-called background aerosol (Junge, 1963) was expected
60 to be most clearly visible, far away from the northern hemispheric anthropogenic emission
61 centers at lower latitudes. Episodic and localized occurrences of high concentrations of
62 ultrafine particles, (here defined as particles with diameters < 100 nm), in the summer Arctic
63 were explained by rare import of polluted air from lower latitudes (Flyger and Heidam, 1978;
64 Heintzenberg and Larssen, 1983) or hypothetical anthropogenic sources in the Arctic
65 (Jaenicke and Schütz, 1982).

66 With the advent of sensitive condensation nuclei counters (Agarwal and Sem, 1980) and
67 differential mobility analyzers (Knutson and Whitby, 1975b, a) more details became visible in
68 the Arctic sub-micrometer aerosol. High numbers of ultrafine particles were observed in
69 connection with fog passages (Lannefors et al., 1983) and chemical aerosol information
70 indicated a regional – possibly biogenic – particle sources in the summer Arctic
71 (Heintzenberg, 1989). The high molar ratios of methane sulfonate, (MSA), to non-sea salt
72 sulfate, (nssSO_4^{2-}), of 0.28 in the Arctic summer aerosol found by Heintzenberg and Leck
73 (1994) substantiated the biogenic source of the particles.

74 The establishment of long-term Arctic aerosol monitoring at the fringes of the pack ice in
75 Alaska (e.g., Polissar et al., 1999), Canada (e.g., Norman et al., 1999; Willis et al., 2016), and
76 on Spitsbergen (e.g., Tunved et al., 2013) revealed more details of potential sources of the
77 summer aerosol, in particular their connection to the marine biosphere in the Arctic. The
78 unique series of systematic aerosol studies in the central Arctic north of 80°N onboard the
79 Swedish icebreaker *Oden* in 1996 led to the formulation of a new hypothesis concerning a

80 specific process of marine biogenic particle formation (Leck and Bigg, 1999). The marine
81 biogenic particles involved behaved as polymer gels and originated in the surface microlayer
82 (SML) of the ocean, (Orellana et al., 2011b), from the activity of sea-ice algae,
83 phytoplankton and, perhaps, bacteria. The new particle events were reported to occur as
84 simultaneous enhancement of particle number concentrations in the whole size-range below
85 50 nm, and not with the prototypical “banana growth” (Kulmala et al., 2004). Two more
86 *Oden* cruises in 2001 and 2008 yielded results that were partly contradicting (Held et al.,
87 2011b; Held et al., 2011a), partly supporting the SML hypothesis (Leck et al., 2013; Karl et
88 al., 2013; Orellana et al., 2011b; Leck and Bigg, 2010). The synopsis of the results of four
89 *Oden* cruises of Heintzenberg et al. (2015) identified geographic regions of new particle
90 formation (NPF) in the inner Arctic while stressing the importance of recent open water and
91 related biological activity in the sea in transects by air masses with new particle formation
92 over the central Arctic.

93 Two years of aerosol size distributions from Mt. Zeppelin, Spitsbergen and Alert, both
94 located at the fringes of the central pack ice, were analyzed by Croft et al. (2016a) with a
95 global aerosol geophysics model. They discuss classical new-particle nucleation, coagulation
96 scavenging in clouds, scavenging by precipitation, and transport in order to explain the annual
97 cycle of the Arctic aerosol. Croft et al. (2016a) find two seasonal maxima in their modeled
98 particle nucleation rates, one in March, and one in July. In spring, their simulated NPF occurs
99 mainly in the free troposphere, whereas in summer, it occurs also in the planetary boundary
100 layer. More recently, Croft et al. (2016b) state that ammonia from seabird-colony guano is a
101 key factor contributing to bursts of newly formed particles, which are observed every summer
102 in the near-surface atmosphere, at least at Alert, Nunavut, Canada. Earlier, the results of
103 studies with another global aerosol model by Browse et al. (2014) suggested that the potential
104 increase in NPF in the Arctic with potential increases in cloud condensation nuclei is

105 compensated by wet scavenging. They also state that scavenging by pre-existing large
106 particles suppresses NPF-events.

107 Based on three years of data from the two Arctic sites Thule and Ny-Ålesund (gruvebadet)
108 Becagli et al. (2016) examined the sources and environmental factors controlling the
109 biological aerosol component MSA. Their analysis included satellite-derived Chlorophyll-*a*
110 (an indicator of phytoplankton biomass), oceanic phytoplankton primary productivity, (PPP),
111 and sea ice. Whereas they found good correlations between MSA, PPP and sea ice, (the latter
112 two being closely related), their data did not allow any statements on NPF processes.

113 To date the longest record of sub-micrometer number-size distributions of the Arctic
114 aerosol down to 5 nm particle diameter and below has been accumulated on Mt. Zeppelin,
115 Spitsbergen (Tunved et al., 2013; Heintzenberg and Leck, 1994). For the ten years from 2006
116 through 2015 a total of 63936 quality-controlled hours of aerosol data are available, i.e.
117 during 73% of all hours of the ten years. In the present study we exploit this formidable data
118 set in a search for processes forming new particles. An important first step in this work was
119 formulating completely objective criteria for the identification of events. In the relatively
120 clean Arctic environment we do not expect the classical nucleation and growth events as
121 frequently observed over the continents, (cf. Kulmala et al., 2004), to dominate. Thus, we
122 refrained from applying the objective search algorithm formulated by Heintzenberg et al.,
123 (2007) for this “Banana-type” of events. Instead we formulated new objective search
124 algorithms allowing several potential types of new particle formation events or formation
125 processes. With a host of complementary atmospheric and surface physical, chemical, and
126 biological information a large number of NPF-events identified with these algorithms will be
127 analyzed in the following chapters.

128

129

130

131 **2. Database**

132

133 The Mt. Zeppelin observatory

134

135 Situated at the top of Mt Zeppelin, Svalbard (78° 56'N, 11° 53'E), the Zeppelin observatory
136 offers a unique possibility to study the characteristic features of Arctic atmospheric
137 constituents such as trace gases and aerosol particles. At a height of 474 m a.s.l. the station is
138 located near the top of the local planetary boundary layer and represents remote Arctic
139 conditions. The closest source of pollution, the small community of Ny-Ålesund, is located
140 ~2 km north of the station
141 (http://www.esrl.noaa.gov/psd/iasoa/sites/default/files/stations/nyalesund/nyalesund_site.jpg).

142 However, the elevation difference and typical wind patterns largely prevent pollution from
143 nearby sources to reach the Zeppelin Observatory. The dominating wind pattern is east-
144 southeast katabatic flow from Kongsvegen glacier or from northwesterly directions as
145 channeled by the Kongsfjord (Beine et al., 2001; Heintzenberg et al., 1983). The station itself
146 was initially established in 1991, and is owned by the Norwegian Polar Research Institute
147 (NP). The Norwegian Institute for Air Research (NILU) is responsible for the coordination of
148 the scientific program.

149

150

151 **2.1 Physical aerosol data**

152

153 After a period of continuous aerosol measurements by the Department of Meteorology,
154 Stockholm University in the early 1990ties, (Heintzenberg and Leck, 1994), the Department
155 of Analytical Chemistry and Environmental Science, Stockholm University, initialized
156 observations of the aerosol number size distribution in mid-2000. Originally, the system

157 consisted of a single differential mobility analyzer system, (DMPS), consisting of a medium-
158 size Hauke-type differential mobility analyzer, (DMA), together with a TSI 3760
159 condensation particle counter, covering diameters between 20 and ~500nm. From 2006 on
160 the particle size range was widened covering particle sizes between 10 and 790 nm. In 2005,
161 the rain-cover over the inlet was replaced. Initially, the instrument inlet was of a PM10 type,
162 removing particles or hydrometeors with diameters $>10\ \mu\text{m}$ from the sampled air stream.
163 During a substantial renewal of the Stockholm University equipment in 2010-2011, both inlet
164 and DMPS system were replaced.

165 Since then, the DMPS-system utilizes a custom-built twin DMA-setup comprising one
166 Vienna-type medium DMA coupled to a TSI CPC 3010 covering sizes between 25-800 nm
167 and a Vienna-type long DMA coupled with at TSI CPC 3772 covering sizes between 5-60
168 nm. The size distributions from the two systems are harmonized on a common size grid and
169 then merged. Both systems use a closed-loop flow setup. The current inlet hat is of whole air
170 type, complying with EUSAAR¹ standard for high altitude or Arctic sampling conditions. In
171 the current setup, the inlet is operated with a flow of ca. 100 liters per minute, (lpm). Laminar
172 flow conditions apply throughout the sampling lines. Outside of the station, the inlet
173 temperature is kept above 0°C using active heating. Inside the station the temperature
174 increases gradually to room temperature (maximum temperature reaches ca. 25 °C, but
175 remains typically around 20°C). Relative humidity, (RH) and temperature are internally
176 monitored and measurements are maintained at dry conditions with $\text{RH} < 30\%$. The system is
177 regularly checked with latex spheres and flow controls. The recorded data are manually
178 screened and crosschecked with other available observation as in Tunved et al. (2013). If
179 inconsistencies were found between the different datasets, further investigation was

¹ EUSAAR (European Supersites for Atmospheric Aerosol Research) is an EU-funded I3 (Integrated Infrastructures Initiatives) project carried out in the FP6 framework of the specific research and technological development gram "Structuring the European Research Area - Support for Research Infrastructures", (<http://www.eusaar.net/>).

180 performed to exclude data that were identified as affected by instrumental errors. Using the
181 instrumental logbook, periods of local activity potentially influencing the sampling were also
182 excluded from the dataset. During the years 2006 – 2010 no particles below ten nanometers
183 in diameter were recorded. From 2011 on four more diameter bins down to 5 nm were
184 included and a different diameter array was utilized. To allow for a synopsis of all years all
185 size distributions were interpolated on the pre-2011 diameter array and all integrals of the size
186 distribution over particle diameter were taken over the joint diameter range 10 to 631 nm. For
187 the pre-2011 years the data at the four size channels below 10 nm were flagged as missing.
188 However, whenever results cover the complete time series the resulting number
189 concentrations in the four first channels covering the years 2011 – 2015 are carried along.

190 For the identification of NPF in terms of particle growth the parameter D50 in nanometer
191 was calculated as the number median diameter of particles smaller than 50 nm but larger than
192 10 nm, i.e. 50% of all particles below that size are smaller than D50. Besides this parameter
193 Table 1 lists nine integral particle parameters, which are utilized in the NPF-search
194 approaches or in the interpretation of results. These aerosol parameters quantify total particle
195 number, (NTO), and particle numbers in sub-ranges of the number size distribution such as
196 N25, quantifying the total number of particles between ten and 25 nm.

197 Following the concept developed by Pirjola et al., (1999), and Kulmala et al., (2001) we
198 calculated the condensation sink, (CS, s^{-1}), as a parameter with which the probability of new
199 particle formation from the gas phase and the necessary amount of condensable vapor can be
200 estimated. We utilized number size distributions, pressure and temperature taken from our
201 database for this calculation.

202

203

204

205

206 2.2 Chemical aerosol data

207

208 For the interpretation of NPF-events we employed chemical information derived from the
209 analyses of high volume particle samples taken by the Norwegian Institute for Air research,
210 (NILU). A high volume sampler (PM10) was used to collect samples for a quantitative
211 determination of sodium, (Na^+), sulfate, (SO_4^{2-}) and MSA (CH_3SOO^-). The sampler collected
212 material for analysis in one to three days. Blank samples were obtained by mounting the
213 glass fiber filters at the sampling site with the same sampling period but without air passing
214 through. Na^+ and SO_4^{2-} were analyzed by NILU and have been downloaded for the present
215 study from the EBAS database (<http://ebas.nilu.no>), which list details about the sampling
216 technique and the sampling protocol. Nss SO_4^{2-} was determined from total sulfate correcting
217 for sea salt sulfate as $0.25 \times \text{Na}^+$, (Keene et al., 1986).

218 MSA was analyzed at the laboratory of the Department of Meteorology, Stockholm
219 University. To allow for subsequent chemical determinations the ambient samples and blanks
220 were carefully handled in a glove box (free from particles, sulfur dioxide and ammonia). At
221 the time of the chemical analyses, still in the glove box, the substrates were extracted (in
222 centrifuge tubes) with 60 cm^3 deionized water (Millipore Alpha-Q, conductivity $18 \text{ M}\Omega\text{cm}$).
223 The extracts were thereafter analyzed for weak anions by chemically suppressed ion
224 chromatography (IC, Dionex ICS-2000) using Dionex AG11/AS11 columns. In order to trap
225 carbonates and other ionic contaminants a Dionex ATC-1 column was used before the
226 injection valve. The injection volume was $50 \mu\text{dm}^3$. Quality checks of the IC-analyses were
227 performed with both internal and external reference samples (Das et al., 2011). The analytical
228 detection limits obtained for the various ions, defined as twice the level of peak-to-peak
229 instrument noise, was $0.0001 \mu\text{eq dm}^{-3}$ for MSA. The overall analytical accuracy was better
230 than 1.5%.

231

232 **2.3 Back-trajectories and meteorological data**

233

234 For every hour during the ten years 2006 through 2015 three-dimensional back trajectories
235 have been calculated arriving at 474 m at Mt. Zeppelin. The trajectories have been calculated
236 backward for up to ten days using the HYSPLIT4 model (Draxler and Rolph, 2003) with
237 meteorological data from the Global Data Assimilation System with one-degree resolution
238 (GDAS1). Trajectories extending backwards for ten days are inaccurate at origin due to the
239 trajectory uncertainty of 25-30% of its length, (Stohl, 1998). More information about the
240 GDAS dataset can be found at Air Resources Laboratory (ARL), NOAA
241 (<http://ready.arl.noaa.gov>), from which the meteorological data were downloaded.

242 During the analyzed time period meteorological records at the Mt. Zeppelin station are
243 rather limited in quality and were frequently interrupted. There are no precipitation
244 measurements and wind measurements are strongly influenced by the station building and by
245 the local topography. In order to have an internally consistent, and unbroken meteorological
246 record we utilized hourly meteorological parameters at trajectory arrival times as calculated
247 by the HYSPLIT4 model. We emphasize that their accuracy depends on the quality of the
248 meteorological model inside HYSPLIT4 and the accuracy and representativeness of the
249 meteorological fields utilized by the model. Of the local meteorological record air
250 temperature was considered the most reliable and thus explored in a comparison of trajectory
251 calculated and modeled meteorological data. When comparing the 42600 contiguous hourly
252 records from 2008-01-01 until 2012-11-10 the average ratio of measured and calculated
253 temperatures is 0.98, with a coefficient of determination of 0.96. The utilized model
254 parameters are listed in Table 1.

255 As an additional parameter we evaluated the vertical air movement of the trajectories
256 during the last hour before arrival by subtracting the trajectory height one hour before arrival

257 at the arrival height of 474 meter. The resulting vertical displacement parameter, DZ, is given
258 in meters per hour. Positive values of DZ indicate a lifting of the air.

259 The most important missing meteorological information concerns the local cloud cover.
260 No direct recording was available of times during which the station was in clouds. The
261 closest available cloud instrument is a ceilometer operated by the Alfred Wegener Institute
262 (AWI) at their Koldewey Station in Ny-Ålesund, i.e. in the valley below Mt. Zeppelin, some
263 2.8 km of horizontal distance from the position of the mountain station. From the one-minute
264 records of the ceilometer we derived hourly values of the 25% percentile of cloud base, which
265 was used as an indicator for the Zeppelin station being in cloud. This ceilometer parameter is
266 listed as C25 in Table 1.

267 Precipitating clouds scavenge the planetary boundary layer and thus reduce the available
268 particle surface as condensation sink of particle precursors. As a consequence nucleation
269 from the gas phase may be facilitated (Tunved et al., 2013). As in Tunved et al. (2013) we
270 utilized the HYSPLIT-modeled precipitation along the back trajectories. Sums of
271 precipitation, (SP, see Table 1), were calculated along each back trajectory and will be
272 referred to as SP1 (during the last day), SP2 (during the last but one day), and SP5 (during
273 days three to five) before arrival at Mt. Zeppelin.

274

275

276 **2.4 Marine biological data**

277

278 The biologically active marginal ice zone is a major natural source of sulfur in the Arctic
279 summer atmosphere, (Leck and Persson, 1996b, a), and Wiedensohler et al. (1996), indicated
280 a potentially important role of dimethyl sulfide (DMS) in regional new particle formation.
281 DMS emissions from the sea have long been proposed to control new particle formation in the
282 marine boundary layer, (Charlson et al., 1987), which builds on DMS_{aq} being transported via

283 turbulence and diffusion to the sea-air interface, represented by the transfer velocity, which in
284 turn depends on sea-surface temperature, salinity, and wind speed, (Liss and Merlivat, 1986).
285 Once in the atmosphere DMS_g is photochemical oxidized via intermediates such as sulfuric
286 acid and methane sulfonic acid, (Ayers et al., 1996), which eventually leads to the formation
287 of aerosol nssSO_4^{2-} and MSA. The products of the photochemical oxidation of DMS the ratio
288 $\text{MSA}/\text{nssSO}_4^{2-}$ show a temperature dependence (Bates et al., 1990), favoring MSA in the cold
289 Arctic environment (Karl et al., 2007).

290 Dimethyl sulfide in the ocean (DMS_{aq}) is produced through the degradation of its algal
291 precursor dimethylsulfoniopropionate (DMSP) by microbial food webs, (Simó, 2001). At
292 high latitudes, total DMSP (DMSPt) and therefore DMS_{aq} , essentially follows the seasonal
293 cycle of phytoplankton biomass, (Lana et al., 2012). DMSPt is defined as the sum of
294 $\text{DMSP}_{dissolved}$ and $\text{DMSP}_{particulate}$ concentration. Yet, the amount of DMSPt per unit
295 phytoplankton biomass may vary depending on species composition and physiological state,
296 (Keller et al., 1989).

297 The dissolved organic carbon (DOC) concentrations in surface waters of the high Arctic
298 Ocean are up to ten times higher than in any other ocean basin and closer in range to DOC
299 levels reported for sea ice (Gao et al., 2012). A large fraction of DOC spontaneously
300 assembles into polymer gels: polysaccharide forming hydrated calcium bonded three-
301 dimensional networks to which other organic compounds, such as proteins and lipids, are
302 readily bound. The assembly and dispersion of the polysaccharide molecules can be affected
303 by environmental parameters, such as UV-B radiation (280-320nm) dispersing or inhibiting
304 gel formation, and/or pH and temperature inducing gel volume phase changes (swelling and
305 shrinkage). In the study of Orellana et al., (2011b), the swelling and shrinking of the
306 polysaccharide networks or polymer gels were also causally related by additions of nano to
307 micromolar levels of DMS and DMSP. High DMSP concentrations have also been measured

308 in the mucilage surrounding prymnesiophyte *Phaeocystis pouchetii* colonies in Arctic waters,
309 representing up to 25% of the total water column DMSP pool, (Matrai and Vernet, 1997).
310 The findings made by Orellana et al., (2011b) were in agreement with previous findings by
311 Orellana et al., (2011a) that high concentrations of DMSP and DMS are stored in the acidic
312 secretory vesicles of the *Phaeocystis* algae where DMSP is trapped within the condensed
313 polyanionic gel matrix until the secretory vesicles are triggered by environmental factors such
314 as temperature to release gels that undergo volume phase transition and expand at the higher
315 pH of seawater. Exocytosis of polymer gels accompanied by elevated DMS and DMSP
316 concentrations suggests the transport of these chemical compounds by the gel matrix.
317 Schoemann et al., (2005) report that *Phaeocystis antarctica* is particularly well adapted to low
318 temperatures, being more competitive than *P. pouchetii* for temperatures between -2 and
319 +2 °C. *Phaeocystis pouchetii*, however, appears to be better adapted to temperatures closer to
320 5 °C. In the Arctic a higher occurrence of the *Phaeocystis pouchetii* would be expected in the
321 northward advection of warm Atlantic water masses around Svalbard.

322 Here we estimated DMSPt at the sea surface using the algorithm described by Galí et al.
323 (2015). The DMSPt algorithm exploits the distinct relationship between DMSPt and
324 Chlorophyll-*a* depending on the light exposure regime of the phytoplankton community. The
325 light exposure regime is defined by the ratio between euphotic layer depth and mixed layer
326 depth (Z_{eu}/MLD). Additional predictor variables used are sea surface temperature (SST) and
327 particulate inorganic carbon (PIC), which is used in the algorithm as a proxy for
328 coccolitophores such as *Emiliania huxleyi*. During late bloom stages, the calcite plates that
329 cover coccolitophore cells (called coccoliths) detach and cause an increase in seawater
330 backscatter that invalidates satellite retrievals of Chlorophyll-*a*. Therefore, inclusion of PIC
331 in the algorithm as a proxy for DMSPt increases data coverage. Although the algorithm was
332 developed for the global ocean, validation results with in situ data indicate that it performs as
333 well or slightly better in Arctic and sub-Arctic waters.

334 The use of remotely sensed DMS_{Pt} as a proxy for marine DMS_{aq} emission is a significant
335 improvement with respect to prior studies that used Chlorophyll-*a* (Becagli et al., 2016;
336 Zhang et al., 2015). Yet, it is not ideal because (i) the ratios DMS_{aq}/DMS_{Pt} in surface
337 seawater are variable, and tend to be higher in high solar irradiance and nutrient-poor
338 conditions typical of summer, (Galí and Simó, 2015), and (ii) even if DMS_{Pt} is a better proxy
339 for DMS_{aq}, the influence of meteorological and sea surface conditions (mainly wind speed
340 and SST) on the sea-air flux of DMS_{aq} is not taken into account. Development is underway of
341 an algorithm for the retrieval of DMS_g concentrations in air and DMS fluxes.

342 The DMS_{Pt} algorithm was run for the 2006-2015 period using daily composites of the
343 Moderate Resolution Imaging Spectroradiometer on the Aqua satellite (MODIS-Aqua) at 4.64
344 km resolution (L3BIN, reprocessing R2014.0) downloaded from NASA's Ocean Color
345 website (<http://oceancolor.gsfc.nasa.gov>). The MODIS variables used include Chlorophyll-*a*
346 concentration derived with the GSM algorithm, (Maritorena et al., 2002), PIC, nighttime SST
347 and Z_{eu} . MODIS nighttime SST was complemented with SST from the Advanced Very High
348 Resolution Radiometer (AVHRR, <https://podaac.jpl.nasa.gov/AVHRR-Pathfinder>) to increase
349 data availability. MLD was obtained from the MIMOC climatology, (Schmidtko et al.,
350 2013), which was linearly interpolated from its original 0.5°x0.5° grid at monthly resolution
351 to the MODIS grid at daily resolution.

352 Satellite remote sensing of biological activity in surface waters requires ice-free and at
353 least part of the time cloud-free. The passive sensing methods of MODIS additionally require
354 a minimum of solar illumination of the scenes (i.e., solar zenith angle < 70°; (IOCCG, 2015)).
355 Consequently, the length of the satellite-observable period used to compute DMS_{Pt} means
356 shortens from all-year-round at latitudes <45° to approximately six months (the spring-
357 summer semester) at 80°N. In addition, the annual DMS_{Pt} map in Fig. 3 excludes all land and
358 ice covered regions. In order to increase data coverage, daily DMS_{Pt} composites were binned
359 to five-day periods and a 46.4 km equal-area sinusoidal grid, (10x10 bins of the original pixel

360 size). The average distance between a trajectory point and the closest center of a MODIS
361 pixel is 18 km.

362 Following the same approach as with the ice data average DMSPt from ocean color data,
363 (OC), along each back trajectory were calculated and will be referred to as OC1 (the last day),
364 OC2 (the last but one day), and OC5 (days three to five) before arrival at Mt. Zeppelin. In
365 this procedure missing data were flagged as such, and were not taken into account.

366

367

368 **2.5 Ice data**

369

370 For the interpretation of events of new particle formation observed during the *Oden* cruises
371 information on pack ice extent under the air masses reaching the sampling points proved
372 crucial (Heintzenberg et al., 2015). Another motivation for utilizing ice data in the present
373 study is the fact that the Svalbard region experiences large seasonal changes in pack ice cover
374 which we expect to have strong effects on emissions of particles and their precursor gases.
375 Thus daily ice concentrations were taken from the NSIDC database (<https://nsidc.org/data>).
376 The irregularly shaped data gap around the pole caused by the inclination of satellite orbits
377 and instrument swath was filled with 100% cover. To each hourly position and data of the
378 back trajectories the ice information in the corresponding maps of ice concentrations were
379 added and displayed in Fig. 2. On average the closest pixel in the ice maps was about 12 km
380 off any trajectory point.

381 In the discussion of results we utilize the complement of ice cover, i.e., the amount of open
382 water because the marine biological processes of interest predominantly take place in the
383 open water, (Leck and Persson, 1996a). As integral parameters average open water, (OW),
384 percentages along each back trajectory were calculated and will be referred to as OW1 (the
385 last day), OW2 (the last but one day), and OW5 (days three to five) before arrival at Mt.

386 Zeppelin. The most solid ice cover is seen in an area reaching from Northeastern edge of
387 Greenland via North Pole to Parry Island. A marginal ice zone extends along the east coast of
388 Greenland to Franz-Josef-Land, and the area between Svalbard and the latter island.

389

390

391 **2.6 ERA-Interim data of sea surface temperature**

392

393 Daily Sea Surface Temperature (SST) data for our study period (2006-2015) were
394 downloaded from the website of the European Centre for Medium-Range Weather Forecasts
395 (ECMWF). A description of the global atmospheric reanalysis, (ERA-Interim), has been
396 given by Dee et al. (2011), and a guide to the products and the download procedures can be
397 found at <http://www.ecmwf.int/en/elibrary/8174-era-interim-archive-version-20>. Briefly,
398 ERA-Interim is an assimilating model reanalysis of the global atmosphere and sea-surface
399 physical parameters covering the data-rich period since 1979. SST data were downloaded at a
400 resolution of approximately 0.56° and regridded onto the same 46 km equal-area sinusoidal
401 grid used for DMSP and cloud fraction, (see below). Ice-covered pixels were screened out
402 prior to the back-trajectory analysis. In the Arctic region, ERA-Interim has been shown to be
403 a top performer among a number of atmospheric reanalyses, (Lindsay et al., 2014).

404

405

406 **2.7 MODIS cloud fraction**

407

408 Persistent cloud cover limits PPP in Arctic and Sub-arctic seas, (Bélanger et al., 2013), and,
409 as mentioned above, irradiance at the sea surface, which is largely controlled by cloudiness,
410 influences $\text{DMSP}_{\text{dissolved-to-DMS}_{\text{aq}}}$ conversion. Boundary layer clouds are known to be
411 additional controllers of the surface aerosol (Heintzenberg, 2012). In the summer Arctic low

412 level clouds and fogs are widespread (Warren and Hahn, 2002). Both scavenging and new
413 particle formation have been observed in connection with low clouds and fog passages
414 (Lannefors et al., 1983; Heintzenberg and Leck, 1994; Leck and Bigg, 1999; Heintzenberg et
415 al., 2006; Karl et al., 2013). Beyond the cloud base derived from the ceilometer we have no
416 other in situ local or regional cloud information. Thus, we utilize satellite-derived cloud
417 information.

418 Daily Level-3 global cloud fraction with one-degree resolution was downloaded from
419 NASA website (<http://modis-atmos.gsfc.nasa.gov>, Hubanks et al., 2015) and extracted for our
420 region of interest. Briefly, level 3 images correspond to the aggregation of all level 2 images
421 (1 km resolution) available within the one-degree resolution grid. For a given L2 scene, each
422 pixel is assigned a value of 1 (cloudy) or zero (clear sky), and then the individual scene values
423 are averaged over a 24-hour period. Note that a given pixel can be revisited up to six or seven
424 times in the course of a day at high latitudes. Finally, the daily composites were re-projected
425 to 46.4 km pixels to match the spatial resolution of DMSPt. The average distance between a
426 trajectory point and the closest MODIS pixel was 18 km.

427 The cloud fraction CF as well as other cloud properties from MODIS have been
428 extensively used, for instance to study the global spatial and temporal distribution of clouds
429 over the last decade (e.g., King et al., 2013). Several studies have also successfully
430 performed validation by comparison with in situ data (e.g., An and Wang, 2015) which
431 demonstrated the ability of the MODIS-aqua sensor to retrieve cloud cover.

432 Following the same approach as with the ice data and DMSPt, average cloud fractions,
433 (CF, see Table 1), along each back trajectory were calculated and will be referred to as CF1
434 (the last day), CF2 (the last but one day), and CF5 (days three to five) before arrival at Mt.
435 Zeppelin. Missing data are flagged as was done with DMSPt data.

436

437

438 3. Three approaches to identifying events of new particle formation

439

440 There are no definitive and no generally accepted methods to identify or predict NPF-events
441 in atmospheric time series of aerosol data. Thus, in the present study we explored different
442 approaches with varying degrees of complexity to identify such events. We emphasize that
443 none of these approaches explicitly is connected to diel cycles such as in Dal Maso et al.,
444 (2005) or makes any assumptions about the time of day during which new particle formation
445 occurs. Three objective search algorithms were written in FORTRAN to analyze the time
446 series of hourly records of aerosol parameters in search of new particle formation:

- 447 1. The simplest approach of upper percentiles (PCT-approach), assumes that NPF-events are
448 characterized by extremely high concentrations of small particles in terms of N25 (see
449 Table 1). The key parameter characterizing each PCT-event was the value of N25
450 averaged over a fixed number of hours, ($N25_{av}$), after the nominal start of an event, (see
451 below). With $N25_{av}$ also a nominal length of PCT-events was defined as the number of
452 hours after the start of an event by which N25 sank to less than half of $N25_{av}$.
- 453 2. The more specific approach of diameter growth (DGR-approach) builds on the temporal
454 development of the particle size distribution in terms of a systematic growth of the
455 diameter D50 (see section 4.1) to find the classical “Banana Type” of NPF-event,
456 (Kulmala et al., 2004). The key parameter characterizing each DGR-event was the average
457 growth of D50 during the nominal event length NUC, (see below). For this approach the
458 nominal length of events was reached when the running two-hour average growth fell
459 below the value one.
- 460 2. The most complex approach of multiple-size events, (MEV-approach), searches for events
461 with concurrent appearance of concentration increases in several size classes below 60 nm
462 diameter (Karl et al., 2013; Leck and Bigg, 2010). The key parameter characterizing each
463 MEV-event was the relative concentration increase averaged over the chosen size classes

464 below 60 nm during the nominal event length NUC, (see below). As with PCT-events a
465 nominal length of MEV-events was defined as the number of hours after the start of an
466 event by which N25 sank to less than half of N25_{av}.

467

468 Three time-related parameters were commonly defined for all three approaches:

469 1. Nominal NPF-event length, (NUC) was nine hours.

470 2. Pre-event periods, (PRENUC), from which increases in diameters or number
471 concentrations were calculated, were six hours.

472 3. Reference periods, (REF), before PRENUC and after NUC periods were defined in order
473 to compare event and pre-event data with non-event conditions. Each of these reference
474 periods had the length of half the sum of pre-event plus event time periods, making the
475 total reference time period of each event as long as that of the event itself.

476 Besides these common characteristic lengths individual fixed thresholds were chosen and
477 discussed below for each approach in order to generate at least 200 unique events per
478 approach, (see Table 2).

479 The aerosol data used to define the NPF-events were complemented by a large number of
480 environmental parameters. The primary temporal resolution of the environmental parameters
481 was between one minute (C25, cf. Table 1) and five days (DMSPt, cf. Table 1). C25 was
482 calculated as 25% percentile on an hourly basis. The parameters with resolutions higher than
483 an hour (OW, CF, and OC, cf. Table 1) were evaluated along the hourly back trajectories.
484 While this procedure yielded hourly varying results even of OW, CF, and OC it has to be kept
485 in mind that this hourly variability is the result of hourly resolved trajectories traversing the
486 grid; the low primary temporal resolutions of the OW, CF, OC, and chemical parameters
487 remain. For these slowly varying parameters the REF periods before and after the events
488 were extended to one day beyond the longest primary resolution, i.e., six days.

489 For two reasons the three search algorithms may yield temporarily redundant results, i.e.,
490 they may identify the same events. One, they go independently through the same time series
491 of aerosol data, possibly causing inter-approach redundancy. Two, each algorithm goes
492 through the time series hour by hour, thus allowing for temporal overlap of events found by
493 each approach, (intra-approach redundancy).

494 The three types of events were assumed to be mutually exclusive and potentially being
495 caused by different sets of conditions for new particle formation. Thus, a FORTRAN
496 procedure was developed to eliminate both intra and inter-approach redundancy while
497 maintaining a maximum of identified NPF-events. To remove intra-approach redundancy the
498 procedure identifies overlapping events within each approach. Of each ensemble of such
499 overlapping events the one with the strongest key parameter of the respective approach
500 (growth of D50, or concentration increases as defined above) is retained. Next, inter-
501 approach redundancy is addressed by the procedure. However, there is no unique solution to
502 the problem of the partly redundant three time series of events. In order to avoid any
503 preference of one or several types of events in the tests of inter-approach overlap pairs of
504 events of different approaches are chosen at random and compared for overlap. This random
505 comparison is done as often as the product of the number of events of the three approaches.
506 This rather time-consuming random test yields stable numbers of non-overlapping events
507 within less than one percent, irrespective of the order in which the events of the three
508 approaches were arranged for the test. By removing intra and inter-approach redundancy in
509 the first two steps of the procedure a number of time periods will be “freed”. Consequently,
510 in a last step, the procedure tries to fill the “freed time periods” non-redundantly with events
511 of the three approaches that had been eliminated in the first two steps. Table 2 collects total
512 numbers and unique numbers of events for each approach. In the rest of the paper only non-
513 redundant events will be discussed. The total number of new particle formation events will
514 be shortened to TNPF.

515 3.1 The upper percentile of N25 (PCT-approach)

516

517 Events of new particle formation were identified by time periods in which N25 was
518 consistently, i.e. on average for three hours, above a set threshold. With a threshold of the
519 93%-percentile (170 cm^{-3}) 4143 PCT-events were identified in the total data set, only 240 of
520 which were unique because most of them overlapped with event or pre-event times of the
521 other two approaches. Average N25 during these unique events was 330 cm^{-3} and the average
522 length of events $4 \pm 0.9 \text{ h}$, (one standard deviation).

523 Fig. 4, (top), shows the average temporal development of the relative size distributions for
524 the unique PCT-events as in the results in Karl et al. (2013), i.e. relative concentrations were
525 formed by dividing the absolute number concentrations by the average total number during
526 the six-hour pre-event time periods. The events are characterized by a nearly monomodal
527 distribution around 20 nm that broadens somewhat around the nominal start of the events.
528 During the last three hours before the events D50 decreased slightly and returned to the pre-
529 event level during the nine NUC hours.

530 In connection with PCT-events average aerosol parameters NTO through N300 showed an
531 average increase by a factor of 2.2 during PRENUC-periods, which was maintained on an
532 average level of 1.5 during the events. The aerosol-chemical parameters Na^+ , nssSO_4^{-2} , and
533 MSA were on an average level of 20% of their reference value. The average environmental
534 parameters indicate a strong increase by a factor of 14 in solar radiation and a lifting of cloud
535 base before the events. During the events the level of solar radiation was still elevated by a
536 factor of six above its reference value. As a consequence temperature at the station was up by
537 2 – 3 degrees. Precipitation 12 h before trajectory arrival time, (SP12) was a factor of five
538 above reference levels for air arriving during NUC-periods, whereas SP35 to SP5D were
539 below their respective reference levels. Cloud fractions were slightly raised 12 - 48 h before
540 air arrival. Of the ocean parameters more open water was met by trajectories 12 to 24 before

541 their arrival with ocean temperatures 12 to 48 h before trajectory arrival having been up to
542 four degrees warmer than their respective reference values. On average DMSPt-parameters
543 OC24 through OC5D showed were raised by a factor of two above their reference value.

544 In Fig. 5, (left top panel), average trajectory height profiles during PRENUC and NUC-
545 periods are displayed. Widely varying vertical air mass paths occurred before and during
546 PCT-events. Median vertical trajectory paths during PRENUC and NUC times indicated air
547 coming from some 300 m above station level five days ago sinking to about one hundred
548 meters above station level during the last two days before arrival. The upper quartiles of the
549 PCT-height profiles point at strong subsidence before air mass arrival.

550 The right top panel in Fig. 5 maps average horizontal trajectory positions in 12 h steps in
551 months having at least ten PCT-events, i.e., May - September. Filled circles around the
552 trajectory positions comprise 95% of all events. The monthly average horizontal trajectory
553 direction during PCT-events mostly was from the northwest. In June and July the trajectories
554 reached farthest into the multiyear ice cover northeast of Greenland. Only during September
555 the back trajectories covered ice-free and marginal ice areas in the Fram Strait. We note that
556 the five-day back trajectories of PCT-events, (and of the other two approaches as well), stayed
557 within some 800 km of Mt. Zeppelin.

558

559

560 **3.2 The diameter growth (DGR) approach**

561

562 The DGR-approach to identify events of new particle formation builds on the classical
563 concept of particle growth through condensable vapors after an initial nucleation of sub-five
564 nanometer particles that cannot be observed with the available instrumentation, so called
565 “Banana-type” (Kulmala et al., 2004). The respective algorithm utilizes the parameter D50,
566 (see Table 1), and requires a growth of this diameter by at least a factor of 1.5 after the

567 nominal start of an event. With this threshold the algorithm searched through all 87646 hours
568 of the ten-year record and found 1199 DGR-events of new particle formation. After
569 eliminating cases of temporal overlap with the other two approaches 235 unique events of this
570 type remained, (see Table 2). Other or more DGR-events could have been found by
571 shortening the nominal nine NUC hours. For two reasons we refrained from discussing
572 shorter growth periods in the DGR-approach. Maintaining common-length NUC periods
573 facilitated the comparison of results of the three approaches. Furthermore, reducing the
574 growth period would also make PCT and DGR-events ever more similar.

575 In the analysis of atmospheric data and theoretical modeling of NPF-events of type DGR
576 two key parameters are discussed, namely particle formation rate J ($\text{cm}^{-3}\text{s}^{-1}$) and growth rate
577 GR (nmh^{-1}) of particle diameters. For both parameters the measurement protocol by Kulmala
578 et al. (2012) provides specific calculation procedures, (equations. 2, 7, and 9), which we
579 follow in the present study, albeit with the caveat that the one-hour temporal resolution of our
580 time series is far below the ten-minute time resolution that the protocol of Kulmala et al.
581 (2012) requests in order to be able to follow the rapid development of NPF-events.
582 Furthermore, only the 127 DGR-events identified from 2011 on are based on particle size
583 distributions measured down to a diameter of five nanometers.

584 The sizes of newly nucleated aerosol particles are of order 1–2 nm, which is below or near
585 the limit of existing measurement techniques. When the nuclei grow in size their number
586 concentration decreases because of various removal mechanisms. Instead of particle
587 formation rates at the initial nucleus size so-called apparent nucleation rates J_x are often
588 reported, i.e. rates at which new particles appear at some larger observable particle diameter
589 dx . For the present study two apparent nucleation rates are calculated: DGR events of the
590 whole time series have been identified with particle size distributions measured at diameters
591 from 10 nm up through the growth of the number median diameter D_{50} in the size range 10 –
592 50 nm. Thus we calculated J_{22} for these 235 events at the nominal geometric mean diameter

593 of 22 nm. For 127 of these events size distributions reached down to five nanometer
594 diameter, (years 2011 and later). For these events we calculated J11 at the geometric mean
595 diameter 11 nm as representative for the diameter range 5 – 25 nm, which is close to the
596 frequently reported apparent formation rate J10 at 10 nm diameter. Additionally, the two
597 corresponding grow rates GR22 and GR11 were calculated in the respective diameter ranges.

598 Statistics of these four key parameters of the DGR events are collected in Table 3.
599 Depending on the pollution level at the measuring site widely varying values of J10 have been
600 reported. For the polluted subtropical environment of Taiwan Young et al. (2013) give values
601 from 4.4 to 30 $\text{cm}^{-3}\text{s}^{-1}$ whereas Pierce et al. (2014) published values between 0.22 and 0.84
602 $\text{cm}^{-3}\text{s}^{-1}$ from a rural Canadian setting. The latter range is within the range 0.1 – 9.4 $\text{cm}^{-3}\text{s}^{-1}$
603 with a median value of 1.2 $\text{cm}^{-3}\text{s}^{-1}$ reported by Yli-Juuti et al. (2009) for a station in rural
604 Hungary. The two formation rates of the present study cover the range 0.1 – 1.4 $\text{cm}^{-3}\text{s}^{-1}$ for
605 the 25% to 75% percentiles (see Table 3), which covers the range of 0.05 to 0.13 $\text{cm}^{-3}\text{s}^{-1}$ given
606 by Vencaz et al. (2009) for a remote site in the Himalaya. The environmental conditions at
607 the Siberian station Tiksi at the coast of the Laptev Sea may come closest to our Arctic
608 setting. From this site Asmi et al. (2016) published formation rates of 0.01 to 0.41 at an
609 unspecified particle size.

610 In terms of 25% to 75% percentiles the particle growth rates of the present study range
611 from 0.4 to 1.4 nmh^{-1} in the range 5 – 25 nm and 1.0 to 1.8 nmh^{-1} in the diameter range 10 -
612 50 nm, which is near the range of results of 1 – 2 nmh^{-1} derived by Ström et al. (2009) for
613 new particle formation in the lower boundary over Ny-Ålesund, Spitsbergen but considerably
614 lower than the maximum growth rate of 3.6 nmh^{-1} reported by Asmi et al. (2016) for July at
615 the Siberian station Tiksi at the coast of the Laptev Sea. For open ocean new particle
616 formation events over the North Atlantic O’Dowd et al. (2010) report a “typical growth rate”
617 of 0.8 nmh^{-1} , whereas Ehn et al. (2010) give an average growth rate of 3 nmh^{-1} . We note that
618 the average length of DGR-events was 10 ± 1 h, (one standard deviation).

619 The average temporal development of the relative number size distribution during DGR-
620 events is presented in Fig. 4, (center). After a decrease of the sub-50 nm diameter median
621 from about 25 to 16 nm during the six hours before the nominal start of the events D50
622 increases systematically during the following nine NUC hours with somewhat reduced growth
623 towards the end of the event.

624 During the PRENUC-periods particle number concentrations N300, and the condensation
625 sink, (CS), decreased relative to the reference periods before and after the events.
626 Subsequently, during the NUC periods the strongest increases was found for N60.
627 Environmental parameters around air mass arrival showed a strong lifting of cloud base,
628 (C25), and an extremely high increase in solar radiation, (by a factor of 11 during PRENUC
629 and by a factor of 60 during NUC periods). However, 12 h before air arrival precipitation had
630 been up by a factor of 2.5. Cloud fractions were down to about 70% of their reference values
631 24 through 48 h before air arrival. Of the chemical aerosol parameters Na^+ and nssSO_4^{-2}
632 showed an increase of 2.6 and 2.3, respectively. OC12 and OC48 were slightly higher than
633 reference level before and during the events. Sea surface temperatures T24 were raised by
634 nearly one degree whereas earlier SST-values, (T36 – T5D), were up to one degree below
635 reference values.

636 Fig. 5, (left center panel), shows statistics of the vertical air movement before trajectory
637 arrival during DGR-events at Mt. Zeppelin covering a wide range of vertical movements
638 between 200 m and beyond 1500 m height. During the days when elevated DMSPt levels
639 were noted median trajectory heights were six to nine hundred meters. Median trajectories
640 during PRENUC times dipped down to the station level, (474 m a.s.l), about one day before
641 arrival, albeit lifted and subsided again shortly before arrival. Vertical trajectory pathways
642 will be discussed further in Section 4.2.

643 Monthly average trajectory positions and their variability in connection with DGR-events
644 are shown in Fig. 5, (center right panel). The months April through October had at least ten

645 DGR-events per month. As with PCT-events the general trajectory direction was from the
646 northwest, mostly staying for several days over the marginal ice zone between northeastern
647 Greenland and eastern Svalbard. During the earliest month of April with 14 DGR-events the
648 back trajectories reached farthest south into the ice-free parts of the Fram Strait.

649

650

651 **3.3 The Multiple-size approach (MEV)**

652

653 Leck and Bigg (2010) and Karl et al. (2013; 2012) discussed a type of new particle formation
654 that to date only has been reported from the summer Arctic. During these MEV-events high
655 ultrafine particle concentrations appear concurrently in a broad diameter range reaching from
656 under 10 to some 60 nm. We simulated this type in a search that required the concurrent
657 increase of NTO, N20, N40, and N60, (cf. Table 1), as averaged over the first three NUC
658 hours by a factor ≥ 1.6 over their respective averages during the six (PRENUC) hours. Over
659 the ten years of data 1191 such events of this type were identified, 266 of which remained
660 after removal of those overlapping with events of other approaches. During these unique
661 events the average concurrent concentration increase was 4.7 and the average length of the
662 events 12 ± 0.8 h.

663 The concurrent appearance of high concentrations at many particle sizes below 60 nm
664 resembles the nocturnal NPF-events analyzed by Suni et al. (2008) in the Australian
665 Eucalyptus forest and simulated in subsequent chamber experiments (Ristovski et al., 2010;
666 Junninen et al., 2008). We emphasize though that the condensing vapors in the Australian
667 NPF-events originating from terrestrial biogenic emission are quite different from the
668 polymer gels implicated in the Arctic MEV-events and originating from the surface
669 microlayer of the ocean.

670 The bottom part of Fig. 4 shows the average temporal development of relative number size
671 distributions before and during MEV-events. The development before the nominal start of
672 MEV-events is more complex than during the PRENUC-periods of the first two types of
673 events. Intermittently a mode around seven nanometers shows up that broadens and becomes
674 more prominent about two hours before the nominal start of events. The major PRENUC-
675 mode around 25 nm also broadens and becomes more prominent towards NUC. A weak
676 mode exists during PRENUC around 120 nm and hardly any particles beyond 400 nm. D50
677 sinks from 25 to about 20 nm and stays below 25 nm through the MEV-events even though
678 number concentrations increase during the first NUC-hours by more than a factor of five.

679 During NUC-periods all particle number concentrations increased, on average by a factor
680 of 1.6. Average solar radiation also increased by about 90% above reference level during
681 NUC-periods. Of the chemical parameters NSSO_4^{-2} showed an increase by a factor of three
682 during PRENUC and NUC-periods, and MSA a slight increase during PRENUC-periods. On
683 one hand, precipitation 12 h, and 36 to 48 h before trajectory arrival, (SP12, SP48), were
684 above reference levels for air arriving during PRENUC-periods. On the other hand, during
685 PRE, SP24, SP36, an SP5D indicated dry conditions during PRENUC and NUC-periods.
686 Only three to five days before air arrival slightly increased cloud fractions were noted. Sea
687 surface temperatures up to five days before trajectory arrival were on average about one
688 degree lower than their reference values. DMSPt parameters OC12 to OC36 were raised by
689 factors of 1.3 and 1.6 during PRENUC and NUC-periods, respectively.

690 Percentiles of vertical trajectory coordinates prior to and during MEV-events are displayed
691 in Fig. 5, (bottom left panel). During the events, and even stronger during the PRENUC
692 periods median trajectories had been below 500 m for more than four days. Furthermore, the
693 final air approach to Mt. Zeppelin mostly came from below the station level. Upper quartiles
694 of the vertical trajectory positions are substantially lower than with DGR-events. We note,

695 however, that a short excursion above station level occurred in the upper quartiles during the
696 last three hours before arrival.

697 The bottom right panel of Fig. 5 gives the monthly average trajectory positions and their
698 variability in connection with MEV-events. The months April through October had at least
699 ten MEV-events per month. As with the other approaches the general trajectory direction was
700 from the northwest, albeit with stronger swings towards the ice-free areas south of Svalbard
701 early and late in the season, (April, May, and September). Interestingly, the trajectories of the
702 11 MEV-events in October were directed nearly straight north from the North Pole.

703 Summarizing differences and commonalities among the results of the three approaches we
704 can state that the length of the events increases from four to ten and twelve, going from PCT
705 to MEV-events. PCT-events are characterized by lower-than-reference aerosol-chemical
706 parameters. Na^+ and nssSO_4^{-2} show strong increases in the other two types of events: Na^+ in
707 connection with DGR-events and nssSO_4^{-2} in connection with MEV-events. Both, PCT and
708 DGR-events exhibit strong increases in solar radiation. Precipitation before air arrival was
709 raised at varying times in connection with the three types of events. Cloudiness both
710 increased and decreased at varying times before air arrival with the three types of events.
711 Increased open water under the trajectories was strongest with DGR-events and least
712 important with MEV-events. Only in connection with PCT-events strongly raised sea surface
713 temperature were noted before trajectory arrival. DMSpt related ocean parameters were
714 raised to varying degrees and at varying times before all NPF-events, most strongly in
715 connection with PCT-events and least in connection with DGR-events.

716

717

718 **4. Discussion**

719

720 **4.1. Environmental setting**

721

722 The discussion of the results on new particle formation in the Svalbard region builds on the
723 variability of new particle formation and related environmental parameters on scales of
724 months, and days. Fig. 1 gives an overview over the geographic areas which were covered by
725 one, two, and five-day back trajectories to Mt. Zeppelin during the ten years of the present
726 study covering the months March through October. This figure illustrates that air arriving at
727 Mt. Zeppelin during the ten summers of the present study came from widely varying regions
728 from the central ice-covered Arctic via the northern seas and northernmost Scandinavia to
729 Greenland. One-day back trajectories cover a roundish area from the central east coast of
730 Greenland via northern Scandinavia to Franz-Josef-Land, North Pole and back to the north
731 coast of Greenland. Excluding inner Greenland this area is widened by roughly 500 km by 2-
732 day back trajectories and by at least another 500 km by 5-day back trajectories reaching over
733 most of Greenland and the adjacent seas west of Greenland. This is a much wider region
734 from which air may reach Mt. Zeppelin as compared to sites in the inner Arctic as illustrated
735 in Fig. 2 of Heintzenberg et al. (2015).

736 On the path of trajectories to Mt. Zeppelin quite different ice conditions were met (see,
737 Fig. 2). On average North Atlantic open waters reached around West Spitsbergen all the way
738 to Nordaustlandet. Drift ice was passed over by trajectories along the whole east coast of
739 Greenland. One-day trajectories passed over the marginal ice zone from the Fram Strait to
740 Franz-Josef Land but also over more contiguous ice close to the North Pole. At times, with
741 five-day back trajectories, even the marginal ice regions of Baffin Bay and Beaufort Sea were
742 reached.

743 The long-term geographical distribution of DMSPt in Fig. 3 reflects the water conditions
744 for phytoplankton biomass around Svalbard. Directly at the coasts of Greenland and Eurasia
745 increased nutrient availability in coastal and shelf waters (due to continental run-off and
746 enhanced hydrodynamics) cause localized areas of high DMSPt values. The low DMSPt

747 values further out along the coast of Greenland are due to sea ice reaching through the Fram
748 Strait far south, (see Fig. 2). A prominent feature in the regional DMS_{Pt} distribution is the
749 tongue of high DMS_{Pt}, (intense blue color), and thus high phytoplankton biomass east of this
750 area, reaching from Spitsbergen to roughly Jan Mayen that lies within one-day back
751 trajectories. Northward-flowing Atlantic waters, carried by the West Spitsbergen Current,
752 and southward-flowing fresh surface waters from melting ice, and recirculated Atlantic
753 waters, carried by the East Greenland Current (Rudels et al., 2005) are meeting. The layering
754 created by water masses of different density stabilizes the water column and traps
755 phytoplankton cells at well-lit depths. If sufficient nutrients are available, this can lead to the
756 development of large phytoplankton blooms, which can result in high concentrations of
757 DMS_{aq}, (see Fig. 2 in Leck and Persson, 1996a).

758 In the ten-year average cloud fractions systematic differences in cloudiness appear.
759 Depending on transport pathways as identified by the back trajectories, cloudiness varies on
760 the way to Spitsbergen. The ice-covered areas, (cf. Fig. 2), from the east coast of Greenland
761 to Franz-Josef-Land exhibit somewhat lower cloud fractions than the ice-free regions
762 southwest to east of Spitsbergen.

763

764

765 **4.2 Seasonal variability**

766

767 Seasonal changes are discussed in terms of monthly averages taken over the ten-year study
768 period. As expected in Earth's polar regions the seasonal variability of all environmental
769 parameters is very high as exemplified by the solar flux, (SFL), and the air temperature,
770 (TEM), at Mt. Zeppelin in Fig. 6. Due to the seasonal change in cloudiness, (cf. Fig. 7), the
771 seasonal distribution of SFL is not quite symmetrical about midsummer but is skewed slightly
772 towards the cloud minimum in spring. The air temperature, however, does not peak before

773 July and has a broad shoulder into fall and winter. The first, and partly absolute maxima, of
774 the seasonal distributions of NPF-events in Fig. 6 coincide with that of the SFL but then drop
775 of more slowly towards fall than solar radiation. In particular, MEV-events do so and even
776 have their main maximum in August. The occurrence of all NPF-events drops off sharply in
777 October. Whereas May as the first month with larger numbers of events is dominated by
778 PCT-events, followed by DGR and then MEV-events, the contributions of the three NPF-
779 types are reversed in the last month with high NPF-numbers, i.e., September.

780 Fig. 6 clearly shows that the formation of new particles in the Svalbard region is not
781 controlled by the late winter-to-early-spring phenomenon of Arctic haze peaking with highest
782 sulfate-concentrations in March, (cf. Fig. 3 in Heintzenberg, 1989, and Fig. 6), which has a
783 minimum in the total number of NPF-events. This minimum is in contrast with the maximum
784 in new particle formation rates found by Croft et al. (2016a) with their global aerosol model.
785 The high numbers of accumulation mode particles during the Arctic haze months in late
786 winter and spring yield the annual maximum in condensation sink, (CS in Fig. 6), which
787 could quench nucleation events and subsequent growth. Thus, even though photochemistry
788 may produce significant amounts of nucleating material, the freshly formed particles will not
789 grow to stable size before they are removed via either deposition or coagulation as discussed
790 by Tunved et al. (2013) and others. An alternative explanation of the late onset of NPF-
791 events in TNPF in spring lies in the marine biological processes not being activated nearby
792 during the Arctic haze period yet, (Heintzenberg and Leck, 1994).

793 Fig. 7 collects the seasonal variation of environmental parameters as averaged along the
794 back trajectories to Mt. Zeppelin. From their minimum in March-April open water conditions
795 improve until September, after which the pack ice extent under the trajectories rapidly
796 increases again. The widening open water areas are reflected in sea surface temperatures
797 under the trajectories that increase until September before they drop off strongly in October.
798 Consequently, because of its connection to marine biological activity DMSPt increases in the

799 euphotic zone from first photosynthetic light in May until it evens out around July and drops
800 off in October. Largest DMSPt values are reached in the vicinity of Svalbard, (cf. OC12 in
801 July and August in Fig. 7), i.e. considerably later than MSA. The ending of DMSPt-curves in
802 October is due to the lack of data not due to zero-DMSPt. Still, DMSPt concentrations are
803 expected to be low at this time of the year at temperate to polar latitudes due to low
804 phytoplankton biomass and low light exposure, (see Fig. 9 in Galí et al., 2015). In terms of
805 the MODIS-derived cloud fraction cloudiness increases rapidly from its minimum in April
806 and evens out on a plateau of 80 – 90% after July. The spring-minimum in cloudiness is
807 confirmed by the maximum in cloud base as indicated by C25 in Fig. 7. This seasonal
808 distribution of cloudiness does not correspond to the classical picture of near-surface
809 cloudiness that exhibits near cloud-free conditions in winter and mostly overcast with Arctic
810 stratus and fogs during the summer months (Warren and Hahn, 2002; Huschke, 1969). We
811 explain the difference by the specific atmospheric pathways covered by the back trajectories
812 of the present study (cf. Fig. 1). Trajectory-averaged precipitation parameters (SP12-5D in
813 Fig. 7) have minima in the period April – May, from which they increase towards their
814 maxima in fall and winter.

815 The chemical aerosol information derived from the analyses of filters samples has a
816 relatively low temporal resolution of at least one day combined with frequent gaps of several
817 days in between samples. Thus, it cannot directly be related to the time periods of NPF-
818 events. The seasonal distribution of chemical tracers, however, yields important information
819 about new particle formation. Taken over the whole year nssSO_4^{2-} in Fig. 6 is largely
820 anthropogenic, (Heintzenberg and Leck, 1994), and has its maximum during the peak of
821 Arctic haze in March and April and its minimum in August, which does not match any
822 seasonal distribution of NPF-events. We also plotted Na^+ in Fig. 6 as a tracer of the inorganic
823 marine aerosol components sea salt. Na^+ decreases from its winter maximum to its summer
824 minimum in June/July, again without similarity to the NPF-distributions. Instead, the

825 seasonal distribution of Na^+ rather closely follows that of the trajectory-derived wind speed
826 during the last hour before arrival, (not shown in the figure). Wind speed as driver for sea salt
827 production is a well established phenomenon (Blanchard and Woodcock, 1957). After a steep
828 rise in April MSA in Fig. 6 sharply peaks in May and then gradually drops off towards its
829 minimum in October, more gradually than reported for data taken from 1991 to 2004 by
830 Sharma et al. (2012) and earlier than reported by Heintzenberg and Leck (1994), both at the
831 same station. Our seasonal distribution of MSA most closely resembles that of SFL, in Fig. 6,
832 albeit with its peak in May a month earlier than SFL and more strongly skewed towards
833 spring. According to Leck and Persson (1996b) on average the concentrations of the marine
834 biogenic sulfur components, (DMS and MSA), fell with a decline rate of about 30% per week
835 approaching zero values in September explained by reduced ppp (Leck and Persson, (1996a),
836 (consistent with Becagli et al., 2016).

837 As MSA is the only measured aerosol component with exclusively marine biogenic
838 sources, we illustrate its seasonal distribution in greater detail in Fig. 8. In this figure MSA-
839 concentrations measured on Mt. Zeppelin have been extrapolated along 5-day back
840 trajectories, forming monthly average monthly maps of potential MSA-sources during the
841 biologically most active months of March through October.

842 Fig. 8 yields several pieces of information that are relevant to the issue of new particle
843 formation. Early in spring the biological aerosol sources are limited to the North Atlantic and
844 Norwegian Sea. In April the tongue of newly opened waters between Novaya Zemlya and
845 Franz-Josef-Land seemingly is beginning to become biologically active. In May this area
846 widens towards the Barents Sea while the North Atlantic also becomes more active, reaching
847 the Fram Strait. In August two wide potential source regions cover the region from Northern
848 Greenland to the northern end of Scandinavia and the region Barents to Kara Sea. In
849 September even the pack ice north of Svalbard becomes biologically active, (Leck and
850 Persson, 1996a), and shows potential MSA sources, in particular, north of the northern coast

851 of Greenland. Finally, the very weak potential MSA sources in October appear to be situated
852 mainly over the Kara Sea and over the North Atlantic.

853 How do these seasonal distributions compare to those of the NPF-events identified by the
854 three search-approaches defined in Section 3? To address this question we constrained the
855 average seasonal distribution of environmental parameters to those hours that had been
856 identified by the NPF-events of the three approaches. However, none of the individual
857 seasonal distributions of constrained environmental parameters follows closely any of the
858 NPF-events. In particular, the main MSA peak remains in May, thus one month earlier than
859 any peak of the NPF-occurrences. To elucidate further potential differences in the three types
860 of NPF-events we return to the discussion of vertical pathways of related back trajectories,
861 (see Fig. 5). In this figure all three types of NPF-events exhibit a wide range of vertical
862 trajectory paths. As we expect the regional sources of primary particles and particle
863 precursors to be at or near the surface we segregated the NPF-events into subpopulations with
864 back trajectories that remained a given time below 500 m, (roughly station level). In Fig. 9
865 we collected the results concerning the 93 NPF-events that occurred with trajectories under
866 the 500 m limit, i.e., roughly 12% of all events. The top panel shows that the related
867 trajectories not only stayed below 500 m through most of the last five days before arrival but
868 close to the surface until they started rising to the station level about 24 h before arrival. The
869 peak of the sum of event occurrences now coincided with the main MSA peak in May, (see
870 center panel in Fig. 9). For DGR-events the May-maximum was particularly strong whereas
871 the PCT-predominantly occurred in May and June and MEV-events remained clustered
872 around the later part of summer, possibly coupled to SST and DMSPt.

873 A number of environmental parameters indicated substantial deviations from their
874 respective reference values during the months with most frequent occurrence of this sub-
875 population of NPF-events. Strongest deviations were noted for precipitation that was elevated
876 above reference levels two to five days before trajectory arrival, most prominently for DGR-

877 events in May, (by a factor of six 36 h before trajectory arrival). Strong positive deviations in
878 aerosol-chemical parameters only occurred with Na⁺ in PCT and MEV-events, indicating
879 relatively high wind speeds near sea surface in the related air masses. MSA was elevated up
880 to 50% above reference levels only during MEV-events. Elevated levels of DMSpt were
881 noted with all three types of NPF-formation, most prominently for DGR-events 12 to 36
882 hours before which DMSpt was increased by a factor up to 1.7 relative to reference levels.

883 The bottom panel of Fig. 9 gives average trajectory positions in 12 h steps for the months
884 May through September. The circles around the steps comprise 95% of all trajectories.
885 During all months the trajectories stayed in the ice-free and marginal ice zone between Fram
886 Strait and Eastern Svalbard as illustrated by average July ice cover for the ten study years,
887 (for average monthly ice covers cf. Fig. 8). In particular during the earliest and latest months
888 of May and September the trajectories swing farthest south over the open water south of
889 Svalbard. We note that the complementary sub-population of results with trajectories
890 remaining above station level did not yield results that differed strongly from those for the
891 whole population of back trajectories.

892 As a last step in the discussion of seasonal variations in new particle formation a model is
893 formulated that describes the average sum of NPF-events, (TNPF), as a function of three
894 parameters, two of which are directly measurable at the site. With the linear combination of
895 the solar flux, (SFL, Wm⁻²), average sea surface temperature under back trajectories 36 to 48
896 hours before their arrival at the site, (T48, °C), and condensation sink, (CS, 10⁵ s⁻¹):

897

$$898 \quad TNPF = 0.57 \cdot SFL + 15.4 \cdot T48 - 0.69 \cdot CS$$

899

900 TNPF as shown in Fig. 10, can be described within an average deviation of 5% taken over the
901 major months with new particle formation, April - October. Any other of the sea surface
902 parameters describes TNPF less satisfactorily.

903

904

905

906

907 **4.3 Diurnal variability**

908

909 Average hourly occurrence of the three types of NPF-events is plotted in Fig. 11, (top). The
910 three approaches yield rather similar diel variations. From their minimum during the night
911 and early morning hours they reach their maximum occurrence between 12 and 16 h UTC in
912 the afternoon. One might expect the differences between the NPF-types to be due to the
913 requirement of the three types of NPF formation being mutually exclusive. However, this
914 constraint does not exclude that they occur at the same time of day, only that they occur at the
915 same time on the same day.

916 Over the continents new particle formation and growth events of the classical “Banana-
917 type” usually exhibit an increase in measurable precursors such as sulfuric acid shortly after
918 sunrise followed by the detection of increased numbers of nanometer-sized particles between
919 one and two hours later (Kulmala et al., 2004), who deduce a connection to photochemically
920 produced condensable vapors from this daily pattern. In the Svalbard region the sun is up all
921 day between mid-April and the end of August. Consequently we would expect the
922 photochemical production of condensable vapors to have a smaller diurnal amplitude than at
923 lower latitudes, which in turn should even out the diurnal pattern of NPF-events to some
924 degree. Despite the relatively small daily variations in solar elevations the solar flux on Mt.
925 Zeppelin varied on average by more than a factor of five during the sunlit days (see curve
926 SFL in Fig. 11, bottom). The daily maximum of SFL between 12 and 15 UTC coincides well
927 with the average diel change in N25 and NPF-occurrence. As expected in particle growth due

928 to condensable vapors after initial nucleation the daily maximum in N10 precedes that of N25
929 by a few hours.

930 The other process controlling the development of newly formed small particles is the
931 diurnal development of the planetary boundary layer, (Kulmala et al., 2004). We have no
932 data on the daily variation in boundary layer structure over or near the measurement site. The
933 ceilometer data yield the only high-resolution information with some connection to the
934 structure of the planetary boundary layer. During the summer months these data show a
935 consistent daily variation with a jump in most frequent hourly cloud base by about 100 m
936 from about 1570 m after 09 UTC with rather stable values following until 16 UTC, after
937 which cloud base decreases again to values comparable to the early morning hours. The
938 hourly medians of the vertical displacement parameter DZ, (see Fig. 11, bottom), provide a
939 clearer diurnal variation. While being negative throughout the day, i.e. indicating subsiding
940 air during the last hour before arrival at Mt. Zeppelin, DZ indicates the weakest subsidence in
941 early afternoon. We interpret diurnal variation in cloud base and DZ as indicative of local
942 clearing and convection during the day that may be conducive to photochemical processes
943 and mixing in the boundary layer, both of which would be enhancing new particle formation.

944

945

946 **5. Summary and conclusions**

947

948 Three different types of events of new particle formation, (NPF), were identified through
949 objective search algorithms formulated for the present study. The first and simplest algorithm
950 utilizes short-term increases in particle concentrations below 25 nm, (PCT-events). The
951 second one builds on the growth of the sub-50 nm diameter-median, (DGR-events), and is
952 most closely related to the classical “banana-type” of events, (Kulmala et al., 2004) involving
953 the presence of photochemically generated DMS oxidation precursors. The third and most

954 complex, so-called multiple-size approach to identifying NPF-events builds on the hypothesis
955 of Leck and Bigg (2010), suggesting the concurrent production of polymer gel particles at
956 several sizes below about 60 nm, (MEV-events).

957 In this analysis the possibility that sporadic anthropogenic emissions were interpreted as
958 NPF events cannot be excluded completely. However, there are a number of facts arguing
959 strongly against this possibility leading to serious misinterpretation of the data:

960 a) Location and operation of the Mt. Zeppelin station exclude local contamination to a very
961 large extent.

962 b) Manual inspection of the time series by one of the co-authors (PT) further reduced the risk
963 of contaminated data.

964 c) The temporal evolution of MEV events, i.e. concurrent and sustained concentration
965 increases at several particle sizes below 60 nm does not correspond to a typical passage of
966 stack emissions from a large combustion source, (Ogren and Heintzenberg, 1990). Instead, it
967 looks very much like MEV events observed under even stricter constraints on local or
968 regional sources of contamination on icebreaker Oden in the central pack ice area, (Karl et al.,
969 2013), and also looks similar to nocturnal NPF-events in Australian forests, (Suni et al., 2008;
970 Junninen et al., 2008).

971 With these algorithms NPF-events were identified in a ten-year record of hourly number-
972 size distributions taken at the research station on Mt. Zeppelin, Spitsbergen. As a first and
973 general conclusion we can state that NPF-events are a summer phenomenon and not related to
974 Arctic haze, which is a late winter-to-early spring event. The seasonal distribution of the
975 available information on cloudiness does not suggest any direct connection with NPF-
976 formation. The MODIS derived cloud fraction generally is very high (70 – 90%) and rather
977 evenly distributed over the Svalbard region during the months with high frequencies of NPF-
978 events. As already reported in Tunved et al. (2013) NPF-events appear to be somewhat
979 sensitive to the available data on precipitation derived from the trajectory model, in particular

980 when constrained to cases with back trajectories staying below 500 m. In this subpopulation
981 of NPF-events DGR-events show the strongest change in precipitation parameters in
982 connection with new particle formation.

983 The seasonal distribution of solar flux suggests some photochemical control that may
984 affect marine biological processes generating particle precursors and/or atmospheric
985 photochemical processes that generate condensable vapors from precursor gases. Whereas
986 the seasonal distribution of the biogenic MSA follows that of the solar flux it peaks before the
987 maxima in NPF-occurrence. For PCT-events, and more distinctly so for DGR-events, this
988 one-month delay disappears in the subpopulation with back trajectories staying below 500 m.
989 MEV-events, however, maintain their peak occurrence later in summer and early fall.

990 With the limited information on particle size, composition, particle precursors, and
991 environmental conditions no definitive statements can be made about the processes leading to
992 the formation of new particles in the Svalbard region. A host of findings, however, point to
993 varying and rather complex marine biological source processes. The potential source regions
994 for all types of new particle formation appear to be restricted to the marginal ice and open
995 water areas between Northeastern Greenland and Eastern Svalbard. During earliest and latest
996 months with high numbers of NPF-events the back trajectories reach farther south into the
997 open waters of the North Atlantic. Depending on conditions yet to be clarified new particle
998 formation may become visible as short bursts of particles around 20 nm, (PCT-events), longer
999 events involving condensation growth, (DGR-events), or extended events with elevated
1000 concentrations of particles at several sizes below 100 nm, (MEV-events). The seasonal
1001 distribution of NPF-events peaks later than that of MSA and, DGR and in particular of MEV-
1002 events reach into late summer and early fall with much open, warm, and DMSPt-rich waters
1003 around Svalbard, promoting the production of *Phaeocystis pouchetii* together with polymer
1004 gels. Consequently, a simple model to describe the seasonal distribution of the total number
1005 of NPF-events can be based on solar flux, and sea surface temperature, representing

1006 environmental conditions for marine biological activity, and condensation sink, controlling
1007 the balance between new particle nucleation and their condensational growth. Based on the
1008 sparse knowledge about the seasonal cycle of gel-forming marine microorganisms and their
1009 controlling factors we hypothesize that the seasonal distribution of DGR and more so MEV-
1010 events reflect the seasonal cycle of the gel-forming phytoplankton.

1011 Despite the rather small diel changes expected during the summer Arctic there is a
1012 significant diurnal variation in aerosol and environmental parameters. Diurnal distributions
1013 of particle numbers below ten, (N10), and below 25 nm, (N25) follow that of the solar flux
1014 rather closely with a maximum between 14 and 16 UTC with the maximum of N10 occurring
1015 a few hours before that of N25. This delay in maxima may be caused by a slow particle
1016 growth due to photochemically produced condensable vapors. With a peak around noon
1017 MEV-events show the earliest daily peak occurrence with PCT and DGR-events peaking
1018 between 15 and 17 h, more closely to the maximum solar flux. Considering the diurnal
1019 variation in vertical trajectory displacement, (DZ), the early daily maximum in MEV-
1020 occurrence may be simply controlled by boundary layer dynamics.

1021 With the large database of ten years of aerosol data on Mt. Zeppelin enriched by
1022 environmental atmospheric and marine data occurrences, pathways and potential source areas
1023 of different types of new particle formation in the Svalbard region were elucidated by the
1024 present study. More process related information about new particle formation would require
1025 dedicated mechanistic experiments with more detailed information on particle precursors,
1026 ultrafine particles, and boundary layer mixing processes. DGR and MEV-types of new
1027 particle formation seem to be more closely related to near-surface processes. Thus, a low-
1028 level site such as the reopened Station Nord, (Nguyen et al., 2016), would be more suitable
1029 for related mechanistic experiments. Station Nord has the additional advantage of being close
1030 to the potential source regions of DGR and MEV-events identified by the present study.

1031 Acknowledgements

1032

1033 The back trajectories created through the local use of the HYSPLIT4 model developed,
1034 maintained and generously distributed by the Air Resources Laboratory of NOAA were a
1035 backbone of the present study. We are very grateful for the ceilometer data provided by the
1036 Alfred-Wegener- Institute in Bremerhaven/Potsdam and to NSIDC for their providing daily
1037 Arctic sea ice data. Complementing our own chemical analyses of Mt. Zeppelin filter data,
1038 sodium and sulfate results were taken from the EBAS database at the Norwegian Institute for
1039 Air Research (<http://ebas.nilu.no>), for which we are indebted to Anne-Gunn Hjellbrekke and
1040 Wenche Aas. We thank the NASA Ocean Biology Distributed Active Archive Center
1041 (OB.DAAC) for access to MODIS datasets. We are indebted to Yafang Cheng and Zhibin
1042 Wang for providing the algorithm for calculating the condensation sink. MG acknowledges
1043 the receipt of a Beatriu de Pinós post-doctoral fellowship funded by the Generalitat de
1044 Catalunya. Long-term funding of the DMPS measurements was provided by the Swedish
1045 Environmental Protection Agency (Naturvårdsverket). We also thank Norwegian Polar
1046 Institute for substantial support of the field operation on Mt. Zeppelin.

1047

1048

Literature

- 1049
 1050
 1051 Agarwal, J. K., and Sem, G. J.: Continuous flow, single-particle-counting condensation
 1052 nucleus counter, *J. Aerosol Sci.*, 11, 343-357, 1980.
- 1053 An, N., and Wang, K.: A Comparison of MODIS-Derived Cloud Fraction with Surface
 1054 Observations at Five SURFRAD Sites, *J. Appl. Meteor. Clim.*, 54, 1009-1020, 2015.
- 1055 Asmi, E., Kondratyev, V., Brus, D., Laurila, T., Lihavainen, H., Backman, J., Vakkari, V.,
 1056 Aurela, M., Hatakka, J., Viisanen, Y., Uttal, T., Ivakhov, V., and Makshtas, A.:
 1057 Aerosol size distribution seasonal characteristics measured in Tiksi, Russian Arctic,
 1058 *Atmos. Chem. Phys.*, 16, 1271-1287, 10.5194/acp-16-1271-2016, 2016.
- 1059 Ayers, G. P., Cainey, J. M., Granek, H., and Leck, C.: Dimethylsulfide oxidation and the ratio
 1060 of methansulfonate to non sea-salt sulfate in the marine aerosol, *J. Atmos. Chem.*, 25,
 1061 307-325, 1996.
- 1062 Bates, T. S., Johnson, J. E., Quinn, P. K., Goldan, P. D., Kuster, W. C., Covert, D. C., and
 1063 Hahn, C. J.: The biogeochemical sulfur cycle in the marine boundary layer over the
 1064 Northeast Pacific Ocean, *J. Atmos. Chem.*, 10, 59-81, 1990.
- 1065 Becagli, S., Lazzara, L., Marchese, C., Dayan, U., Ascanius, S. E., Cacciani, M., Caiazzo, L.,
 1066 Di Biagio, C., Di Iorio, T., di Sarra, A., Eriksen, P., Fani, F., Giardi, F., Meloni, D.,
 1067 Muscari, G., Pace, G., Severi, M., Traversi, R., and Udisti, R.: Relationships linking
 1068 primary production, sea ice melting, and biogenic aerosol in the Arctic, *Atmos.*
 1069 *Environ.*, 136, 1-15, <http://dx.doi.org/10.1016/j.atmosenv.2016.04.002>, 2016.
- 1070 Beine, H. J., Argentini, S., Maurizi, A., Mastrantonio, G., and Viola, A.: The local wind field
 1071 at Ny-Ålesund and the Zeppelin mountain at Svalbard, *Meteorol. Atmos. Phys.*, 78,
 1072 107–113, 2001.
- 1073 Bélanger, S., Babin, M., and Tremblay, J.-É.: Increasing cloudiness in Arctic damps the
 1074 increase in phytoplankton primary production due to sea ice receding, *Biogeosciences*,
 1075 doi:10.5194/bg-5110-4087-2013, 2013.
- 1076 Blanchard, D. C., and Woodcock, A. H.: Bubble formation and modification in the sea and its
 1077 meteorological significance, *Tellus*, 9, 145-158, 1957.
- 1078 Browse, J., Carslaw, K. S., Mann, G. W., Birch, C. E., Arnold, S. R., and Leck, C.: The
 1079 complex response of Arctic aerosol to sea-ice retreat, *Atmos. Chem. Phys.*, 14, 7543-
 1080 7557, 10.5194/acp-14-7543-2014, 2014.
- 1081 Charlson, R. J., Lovelock, J. E., Andreae, M. O., and Warren, S. G.: Oceanic phytoplankton,
 1082 atmospheric sulphur, cloud albedo and climate, *Nature*, 326, 655-661, 1987.

1083 Croft, B., Martin, R. V., Leaitch, W. R., Tunved, P., Breider, T. J., D'Andrea, S. D., and
1084 Pierce, J. R.: Processes controlling the annual cycle of Arctic aerosol number and size
1085 distributions, *Atmos. Chem. Phys.*, 16, 3665-3682, 10.5194/acp-16-3665-2016, 2016a.
1086 Croft, B., Wentworth, G. R., Martin, R. V., Leaitch, W. R., Murphy, J. G., Murphy, B. N.,
1087 Kodros, J. K., Abbatt, J. P. D., and Pierce, J. R.: Contribution of Arctic seabird-colony
1088 ammonia to atmospheric particles and cloud-albedo radiative effect, *Nature*
1089 *Communications*, 7, 13444, 10.1038/ncomms13444
1090 [http://www.nature.com/articles/ncomms13444 - supplementary-information](http://www.nature.com/articles/ncomms13444-supplementary-information), 2016b.
1091 Dal Maso, M., Kulmala, M., Riipinen, I., Wagner, R., Hussein, T., Aalto, P. P., and Lehtinen,
1092 K. E. J.: Formation and growth of fresh atmospheric aerosols: eight years of aerosol
1093 size distribution data from SMEAR II, Hyytiälä, Finland, *Bor. Env. Res.*, 10, 323-336,
1094 2005.
1095 Das, R., Granat, L., Leck, C., Praveen, P. S., and Rodhe, H.: Chemical composition of
1096 rainwater at Maldives Climate Observatory at Hanimaadhoo (MCOH), *Atmos. Chem.*
1097 *Phys.*, 11, 3743-3755, 10.5194/acp-11-3743-2011, 2011.
1098 Dee, D. P., Uppala, S. M., Simmons, A. J., Berrisford, P., Poli, P., Kobayashi, S., and
1099 Bechtold, P.: The ERA - Interim reanalysis: Configuration and performance of the
1100 data assimilation system, *Q. J. Roy. Meteorol. Soc.*, 137, 553-597, 2011.
1101 Draxler, R., and Rolph, G.: HYSPLIT (HYbrid Single-Particle Lagrangian Integrated
1102 Trajectory) Model access via NOAA ARL READY, NOAA Air Resources
1103 Laboratory, Silver Spring, MD, 2003.
1104 Ehn, M., Vuollekoski, H., Petäjä, T., Kerminen, V.-M., Vana, M., Aalto, P., de Leeuw, G.,
1105 Ceburnis, D., Dupuy, R., O'Dowd, C. D., and Kulmala, M.: Growth rates during
1106 coastal and marine new particle formation in western Ireland, *J. Geophys. Res.*, 115,
1107 n/a-n/a, 10.1029/2010JD014292, 2010.
1108 Flyger, H., and Heidam, N. Z.: Ground level measurements of the summer tropospheric
1109 aerosol in Northern Greenland, *J. Aerosol Sci.*, 9, 157-168, 1978.
1110 Galí, M., Devred, E., Levasseur, M., Royer, S.-J., and Babin, M.: A remote sensing algorithm
1111 for planktonic dimethylsulfoniopropionate (DMSP) and an analysis of global patterns,
1112 *Remote Sens. Environ.*, 171, 171-184, <http://dx.doi.org/10.1016/j.rse.2015.10.012>,
1113 2015.
1114 Galí, M., and Simó, R.: A meta - analysis of oceanic DMS and DMSP cycling processes:
1115 Disentangling the summer paradox, *Global Biochem. Cycles*, 29, 496-515, 2015.

1116 Gao, Q., Leck, C., Rauschenberg, C., and Matrai, P. A.: On the chemical dynamics of
1117 extracellular polysaccharides in the high Arctic surface microlayer, *Ocean Sci.*
1118 *Discuss.*, 9, 215–259, 2012.

1119 Heintzenberg, J., Bischof, W., Odh, S.-Å., and Moberg, B.: An investigation of possible sites
1120 for a background monitoring station in the European Arctic., International
1121 Meteorological Institute in Stockholm, Department of Meteorology, Stockholm
1122 University, Stockholm, Report Nr. AP-22, 74 pp, 1983.

1123 Heintzenberg, J., and Larssen, S.: SO₂ and SO₄ in the Arctic: Interpretation of observations at
1124 three Norwegian Arctic-subArctic stations, *Tellus*, 35B, 255-265, 1983.

1125 Heintzenberg, J.: Arctic haze: air pollution in polar regions, *AMBIO*, 18, 50-55, 1989.

1126 Heintzenberg, J., and Leck, C.: Seasonal variation of the atmospheric aerosol near the top of
1127 the marine boundary layer over Spitsbergen related to the Arctic sulphur cycle, *Tellus*,
1128 46B, 52-67, 1994.

1129 Heintzenberg, J., Leck, C., Birmili, W., Wehner, B., Tjernström, M., and Wiedensohler, A.:
1130 Aerosol number-size distributions during clear and fog periods in the summer high
1131 Arctic: 1991, 1996, and 2001, *Tellus*, 58B, 41-50, 2006.

1132 Heintzenberg, J., Wehner, B., and Birmili, W.: "How to find bananas in the atmospheric
1133 aerosol" New approach for analyzing atmospheric nucleation and growth events,
1134 *Tellus B*, 59, 273-282, 2007.

1135 Heintzenberg, J.: The aerosol-cloud-climate conundrum, *IJGW*, 4, 219-241, 2012.

1136 Heintzenberg, J., Leck, C., and Tunved, P.: Potential source regions and processes of aerosol
1137 in the summer Arctic, *Atmos. Chem. Phys.*, 15, 6487-6502, [10.5194/acp-15-6487-](https://doi.org/10.5194/acp-15-6487-2015)
1138 2015, 2015.

1139 Held, A., Brooks, I. M., Leck, C., and Tjernström, M.: On the potential contribution of open
1140 lead particle emissions to the central Arctic aerosol concentration, *Atmos. Chem.*
1141 *Phys.*, 11, 3093-3105, [10.5194/acp-11-3093-2011](https://doi.org/10.5194/acp-11-3093-2011), 2011a.

1142 Held, A., Orsini, D. A., Vaattovaara, P., Tjernström, M., and Leck, C.: Near-surface profiles
1143 of aerosol number concentration and temperature over the Arctic Ocean, *Atmos.*
1144 *Meas. Tech.*, 4, 1603–1616, 2011b.

1145 Hubanks, P., Platnick, S., King, M., and Ridgway, B.: MODIS Atmosphere L3 Gridded
1146 Product Algorithm Theoretical Basis, Document (ATBD) and Users Guide, 2015.

1147 Huschke, R. E.: Arctic cloud statistics from "air calibrated" surface weather observations,
1148 Rand Corporation Memo. RM 6173-PR, 79 pp, 1969.

1149 IOCCG: Ocean Colour Remote Sensing in Polar Seas, Report 16, Eds. Babin, M., Arrigo, K.,
1150 B elanger, S. and Forget, M.-H., 129 pp, 2015.

1151 Jaenicke, R., and Sch utz, L.: Arctic aerosols in surface air, *Id ojaras*, 86, 235-241, 1982.

1152 Junge, C. E.: Air chemistry and Radioactivity, Academic Press, New York and London, 382
1153 pp., 1963.

1154 Junninen, H., Hulkkonen, M., Riipinen, I., Nieminen, T., Hirsikko, A., Suni, T., Boy, M., Lee,
1155 S.-H., Vana, M., Tammet, H., Kerminen, V.-M., and Kulmala, M.: Observations on
1156 nocturnal growth of atmospheric clusters, *Tellus B*, 60, 365-371, 2008.

1157 Karl, M., Gross, A., Leck, C., and Pirjola, L.: Intercomparison of dimethylsulfide oxidation
1158 mechanisms for the marine boundary layer: Gaseous and particulate sulfur
1159 constituents, *J. Geophys. Res.*, 112, D15304, 10.1029/2006JD007914, 2007.

1160 Karl, M., Leck, C., Gross, A., and Pirjola, L.: A Study of New Particle Formation in the
1161 Marine Boundary Layer Over the Central Arctic Ocean using a Flexible
1162 Multicomponent Aerosol Dynamic Model, *Tellus*, 64B,
1163 doi:<http://dx.doi.org/10.3402/tellusb.v3464i3400.17158>, 2012.

1164 Karl, M., Leck, C., Coz, E., and Heintzenberg, J.: Marine nanogels as a source of atmospheric
1165 nanoparticles in the high Arctic, *Geophys. Res. Lett.*, 40, 3738–3743, DOI:
1166 10.1002/grl.50661, 2013.

1167 Keene, W. C., Pszenny, A. A. P., Galloway, J. N., and Hawley, M. E.: Sea-salt corrections
1168 and interpretation of constituent ratios in marine precipitation, *J. Geophys. Res.*, 91,
1169 6647-6658, 1986.

1170 Keller, M. D., Bellows, W. K., and Guillard, R. R. L.: A survey of dimethylsulfide production
1171 in 12 classes of marine phytoplankton, in: *Biogenic sulfur in the environment*, edited
1172 by: E.S. Saltzman, and Cooper, W. J., American Chemical Society, Washington, D,
1173 167–182, 1989.

1174 King, M. D., Platnick, S., Menzel, W. P., Ackerman, S. A., and Hubanks, P. A.: Spatial and
1175 temporal distribution of clouds observed by MODIS onboard the Terra and Aqua
1176 satellites, *IEEE Trans. Geosci. Remote Sens.*, 51, 3826–3852, 2013.

1177 Knutson, E. O., and Whitby, K. T.: Accurate Measurement of Aerosol Electrical Mobility
1178 Moments, *J. Aerosol Sci.*, 6, 453-460, 1975a.

1179 Knutson, E. O., and Whitby, K. T.: Aerosol classification by electric mobility: apparatus,
1180 theory, and applications, *J. Aerosol Sci.*, 6, 443-451, 1975b.

1181 Kulmala, M., Dal Maso, M., Mäkelä, J. M., Pirjola, L., Väkevä, M., Aalto, P. P.,
1182 Miikkulainen, P., Hämeri, K., and O'Dowd, C. D.: On the formation, growth and
1183 composition of nucleation mode particles, *Tellus*, 53B, 479-490, 2001.

1184 Kulmala, M., Vehkamäkia, H., Petäjä, T., Dal Maso, M., Lauri, A., Kerminen, V.-M., Birmili,
1185 W., and McMurry, P. H.: Formation and growth rates of ultrafine atmospheric
1186 particles: a review of observations, *J. Aerosol Sci.*, 35, 143-176, 2004.

1187 Kulmala, M., Petäjä, T., Nieminen, T., Sipilä, M., Manninen, H. E., Lehtipalo, K., Dal Maso,
1188 M., Aalto, P. P., Junninen, H., Paasonen, P., Riipinen, I., Lehtinen, K. E. J.,
1189 Laaksonen, A., and Kerminen, V.-M.: Measurement of the nucleation of atmospheric
1190 aerosol particles, *Nat. Protocols*, 7, 1651-1667,
1191 <http://www.nature.com/nprot/journal/v7/n9/abs/nprot.2012.091.html> - [supplementary-](#)
1192 [information](#), 2012.

1193 Lana, A., Simó, R., Vallina, S. M., and Dachs, J.: Re-examination of global emerging patterns
1194 of ocean DMS concentration, *Biogeochem.*, 110, 173-182, 2012.

1195 Lannefors, H., Heintzenberg, J., and Hansson, H.-C.: A comprehensive study of physical and
1196 chemical parameters of the Arctic summer aerosol; results from the Swedish
1197 expedition Ymer-80, *Tellus*, 35B, 40-54, 1983.

1198 Leck, C., and Persson, C.: The central Arctic Ocean as a source of dimethyl sulfide: Seasonal
1199 variability in relation to biological activity, *Tellus*, 48B, 156-177, 1996a.

1200 Leck, C., and Persson, C.: Seasonal and short-term variability in dimethyl sulfide, sulfur
1201 dioxide and biogenic sulfur and sea salt aerosol particles in the arctic marine boundary
1202 layer, during summer and autumn, *Tellus*, 48B, 272-299, 1996b.

1203 Leck, C., and Bigg, E. K.: Aerosol production over remote marine areas - A new route,
1204 *Geophys. Res. Lett.*, 23, 3577-3581, 1999.

1205 Leck, C., and Bigg, E. K.: New particle formation of marine biological origin, *Aerosol Sci.*
1206 *Technol.*, 44, 570-577, 2010.

1207 Leck, C., Gao, Q., Mashayekhy Rad, F., and Nilsson, U.: Size-resolved atmospheric
1208 particulate polysaccharides in the high summer Arctic, *Atmos. Chem. Phys.*, 13,
1209 12573-12588, 10.5194/acp-13-12573-2013, 2013.

1210 Lindsay, R., Wensnahan, M., Schweiger, A., and Zhang, J.: Evaluation of seven different
1211 atmospheric reanalysis products in the Arctic, *J. Clim.*, 27, 2588-2606, 2014.

1212 Liss, P. S., and Merlivat, L.: Air-sea gas exchange rates: Introduction and synthesis, in: *The*
1213 *Role of Air-Sea Exchange in Geochemical Cycling*, edited by: Buat-Menard, P.,
1214 Reidel, Norwell, MS, 113-127, 1986.

1215 Maritorena, S., Siegel, D. A., and Peterson, A. R.: Optimization of a semianalytical ocean
1216 color model for global-scale applications, *Appl. Opt.*, 41.15, 2705-2714, 2002.

1217 Matrai, P. A., and Vernet, M.: Dynamics of the vernal bloom in the marginal ice zone of the
1218 Barents Sea: Dimethyl sulfide and dimethylsulfoniopropionate budgets, *Journal of*
1219 *Geophysical Research: Oceans*, 102, 22965-22979, 10.1029/96JC03870, 1997.

1220 Nguyen, Q. T., Glasius, M., Sørensen, L. L., Jensen, B., Skov, H., Birmili, W., Wiedensohler,
1221 A., Kristensson, A., Nøjgaard, J. K., and Massling, A.: Seasonal variation of
1222 atmospheric particle number concentrations, new particle formation and atmospheric
1223 oxidation capacity at the high Arctic site Villum Research Station, Station Nord,
1224 *Atmos. Chem. Phys.*, 16, 11319–11336, 10.5194/acp-2016-205, 2016.

1225 Norman, A. L., Barrie, L. A., Toom-Sauntry, D., Sirois, A., Krouse, H. R., Li, S. M., and
1226 Sharma, S.: Sources of aerosol sulphate at Alert: Apportionment using stable isotopes,
1227 *J. Geophys. Res.*, 104, 11619-11631, 1999.

1228 O'Dowd, C., Monahan, C., and Dall'Osto, M.: On the occurrence of open ocean particle
1229 production and growth events, *Geophys. Res. Lett.*, 37, L19805,
1230 doi:10.1029/2010GL044679, 2010.

1231 Ogren, J. A., and Heintzenberg, J.: Parametric aerosol sampling at low concentration levels,
1232 Department of Meteorology, Stockholm UniversityAA-1, 1990.

1233 Orellana, M. V., Matrai, P. A., Janer, M., and Rauschenberg, C. D.:
1234 Dimethylsulfoniopropionate storage in *Phaecystis* (Prymnesiophyceae) secretory
1235 vesicles *J. Phycol.*, 47, 112-117, 10.1111/j.1529-8817.2010.00936.x, 2011a.

1236 Orellana, M. V., Matrai, P. A., Leck, C., Rauschenberg, C. D., Lee, A. M., and Coz, E.:
1237 Marine microgels as a source of cloud condensation nuclei in the high Arctic, *PNAS*,
1238 108, 13612–13617, 2011b.

1239 Pierce, J. R., Westervelt, D. M., Atwood, S. A., Barnes, E. A., and Leitch, W. R.: New-
1240 particle formation, growth and climate-relevant particle production in Egbert, Canada:
1241 analysis from 1 year of size-distribution observations, *Atmos. Chem. Phys.*, 14, 8647-
1242 8663, 10.5194/acp-14-8647-2014, 2014.

1243 Pirjola, L., Kulmala, M., Wilck, M., Bischoff, A., Stratmann, F., and Otto, E.: Formation of
1244 sulphuric acid aerosols and cloud condensation nuclei: An expression for significant
1245 nucleation and model comparison, *J. Aerosol Sci.*, 30, 1079-1094, 1999.

1246 Polissar, A. V., Hopke, P. K., Paatero, P., Kaufman, Y. J., Hall, D. K., Bodhaine, B. A.,
1247 Dutton, E. G., and Harris, J. M.: The aerosol at Barrow, Alaska: long-term trends and
1248 source locations, *Atmos. Environ.*, 33, 2441-2458, 1999.

- 1249 Rahn, K. A., and Shaw, G. E.: Particulate air pollution in the Arctic: Large-scale occurrence
1250 and meteorological controls, in: *Atmospheric Aerosols and Nuclei*, edited by: Roddy,
1251 F., and O'Connor, T. C., Dept. of Physics, University College, Galway, Ireland 21-27
1252 Sept., 223-227, 1977.
- 1253 Ristovski, Z. D., Suni, T., Kulmala, M., Boy, M., Meyer, N. K., Duplissy, J., Turnipseed, A.,
1254 Morawska, L., and Baltensperger, U.: The role of sulphates and organic vapours in
1255 growth of newly formed particles in a eucalypt forest, *Atmos. Chem. Phys.*, 10, 2919-
1256 2926, 10.5194/acp-10-2919-2010, 2010.
- 1257 Rudels, B., Björk, G., Nilsson, J., Winsor, P., Lake, I., and Nohr, C.: The interaction between
1258 waters from the Arctic Ocean and the Nordic Seas north of Fram Strait and along the
1259 East Greenland Current: results from the Arctic Ocean-02 Oden expedition, *Journal of*
1260 *Marine Systems*, 55, 1-30, 2005.
- 1261 Schmidtko, S., Johnson, G. C., and Lyman, J. M.: MIMOC: A global monthly isopycnal
1262 upper-ocean climatology with mixed layers, *Journal of Geophysical Research:*
1263 *Oceans*, 118, 1658-1672, 10.1002/jgrc.20122, 2013.
- 1264 Schoemann, V., Becquevort, S., Stefels, J., Rousseau, V., and Lancelot, C.: Phaeocystis
1265 blooms in the global ocean and their controlling mechanisms: a review, *Journal of Sea*
1266 *Research*, 53, 43-66, <http://dx.doi.org/10.1016/j.seares.2004.01.008>, 2005.
- 1267 Sharma, S., Chan, E., Ishizawa, M., Toom-Sauntry, D., Gong, S. L., Li, S. M., Tarasick, D.
1268 W., Leaitch, W. R., Norman, A., Quinn, P. K., Bates, T. S., Levasseur, M., Barrie, L.
1269 A., and Maenhaut, W.: Influence of transport and ocean ice extent on biogenic aerosol
1270 sulfur in the Arctic atmosphere, *J. Geophys. Res.*, 117, D12209,
1271 10.1029/2011JD017074, 2012.
- 1272 Simó, R.: Production of atmospheric sulfur by oceanic plankton: biogeochemical, ecological
1273 and evolutionary links, *Trends in Ecology & Evolution*, 16, 287-294, 2001.
- 1274 Stohl, A.: Computations, accuracy and applications of trajectories - A review and
1275 bibliography, *Atmos. Environ.*, 32, 947-966, 1998.
- 1276 Ström, J., Engvall, A.-C., Delbart, F., Krejci, R., and Treffeisen, R.: On small particles in the
1277 Arctic summer boundary layer: observations at two different heights near Ny-Ålesund,
1278 Svalbard, *Tellus B - Chemical and Physical Meteorology*, 61, 473-482, 2009.
- 1279 Suni, T., Kulmala, M., Hirsikko, A., Bergman, T., Laakso, L., Aalto, P. P., Leuning, R.,
1280 Cleugh, H., Zegelin, S., Hughes, D., van Gorsel, E., Kitchen, M., Vana, M., Hörrak,
1281 U., Mirme, S., Mirme, A., Sevanto, S., Twining, J., and Tardos, C.: Formation and

1282 characteristics of ions and charged aerosol particles in a native Australian Eucalypt
1283 forest, *Atmos. Chem. Phys.*, 8, 129-139, 10.5194/acp-8-129-2008, 2008.

1284 Tunved, P., Ström, J., and Krejci, R.: Arctic aerosol life cycle: linking aerosol size
1285 distributions observed between 2000 and 2010 with air mass transport and
1286 precipitation at Zeppelin station, Ny-Ålesund, Svalbard, *Atmos. Chem. Phys.*, 13,
1287 3643–3660, 10.5194/acpd-12-29967-2012, 2013.

1288 Venzac, H., Sellegri, K., Villani, P., Picard, D., and Laj, P.: Seasonal variation of aerosol size
1289 distributions in the free troposphere and residual layer at the Puy de Dôme station,
1290 France, *Atmos. Chem. Phys.*, 9, 1465-1478, 10.5194/acp-9-1465-2009, 2009.

1291 Warren, S. G., and Hahn, C. J.: Cloud climatology, in: *Encyclopedia of Atmospheric*
1292 *Sciences*, edited by: Holton, J. R., Pyle, J., and Curry, J. A., Academic Press, London,
1293 UK, 476-483, 2002.

1294 Wiedensohler, A., Covert, D., Swietlicki, E., Aalto, P., Heintzenberg, J., and Leck, C.:
1295 Occurrence of an ultrafine particle mode less than 20 nm in diameter in the marine
1296 boundary layer of the Arctic summer and autumn, *Tellus*, 48B, 213-222, 1996.

1297 Willis, M. D., Burkart, J., Thomas, J. L., Köllner, F., Schneider, J., Bozem, H., Hoor, P. M.,
1298 Aliabadi, A. A., Schulz, H., Herber, A. B., Leaitch, W. R., and Abbatt, J. P. D.:
1299 Growth of nucleation mode particles in the summertime Arctic: a case study, *Atmos.*
1300 *Chem. Phys. Discuss.*, 2016, 1-31, 10.5194/acp-2016-256, 2016.

1301 Yli-Juuti, T., Riipinen, I., Pasi, A., Nieminen, T., Maenhaut, W., Janssens, A., Claeys, M.,
1302 Salma, I., Ocskay, R., Hoffer, A., Imre, K., and Kulmala, M.: Characteristics of new
1303 particle formation events and cluster ions at K-pusztá, Hungary, *Boreal Environment*
1304 *Research*, 14, 2009.

1305 Young, L. H., Lee, S. H., Kanawade, V. P., Hsiao, T. C., Lee, Y. L., Hwang, B. F., Liou, Y.
1306 J., Hsu, H. T., and Tsai, P. J.: New particle growth and shrinkage observed in
1307 subtropical environments, *Atmos. Chem. Phys.*, 13, 547-564, 10.5194/acp-13-547-
1308 2013, 2013.

1309 Zhang, M., Chen, L., Xu, G., Lin, Q., and Liang, M.: Linking Phytoplankton Activity in
1310 Polynyas and Sulfur Aerosols over Zhongshan Station, East Antarctica, *J. Atmos. Sci.*,
1311 72, 4629-4642, 2015.

1312

1313

1314

Parameter	TR (h)	Explanation
C25	1 min	25% percentile of cloud base from AWI ceilometer (m)
CF12, 24, 36, 48, 5D	24	Average MODIS cloud fraction during the last 12h, 24h, 36, 48h, and days 3-5 before trajectory arrival
D50	1	Number-median diameter of particles < 50 nm diameter
CS	1	Condensation sink (s^{-1})
DZ	1	Vertical trajectory displacement ($m h^{-1}$) during the last hour before arrival
MSA	≥ 1 day	Methane sulfonate ($nmol m^{-3}$)
N10	1	Number concentration of particles up to 10 nm ($>2010, cm^{-3}$)
N20	1	Number concentration between 10 and 20 nm (cm^{-3})
N25	1	Number concentration of particles up to 25 nm (cm^{-3})
N40	1	Number concentration between 20 and 40 nm (cm^{-3})
N60	1	Number concentration between 40 and 60 nm (cm^{-3})
N100	1	Number concentration between 60 and 100 nm (cm^{-3})
N300	1	Number concentration between 100 and 300 nm (cm^{-3})
Na	≥ 1 day	Sodium concentrations ($nmol m^{-3}$)
NCO	1	Number concentration of particles > 300 nm (cm^{-3})
nssSO ₄ ²⁻	≥ 1 day	Non-sea salt sulfate concentrations ($nmol m^{-3}$)
NTO	1	Number concentration of particles ≥ 10 nm, (cm^{-3})
OC12, 24, 36, 48, 5D	120	Average MODIS DMSPt (nmol) during the last 12h, 24h, 36, 48h, and days 3-5 before trajectory arrival
OW12, 24, 36, 48, 5D	24	Average open water (%) during the last 12h, 24h, 36, 48h, and days 3-5 before trajectory arrival
PRE	1	Trajectory precipitation (mm) at arrival
RH	1	Trajectory relative humidity (%) at arrival
SFL	1	Solar flux at trajectory arrival ($W m^{-2}$)
SP12, 24, 36, 48, 5D	1	Accumulated precipitation (mm) during the last 12h, 24h, 36, 48h, and days 3-5 before trajectory arrival
T12, 24, 36, 48, 5D	24	Average sea surface temperature (C) during the last 12h, 24h, 36, 48h, and days 3-5 before trajectory arrival
TEM	1	Trajectory temperature (C) at arrival
WDR	1	Trajectory wind direction ($^{\circ}$) during the last hour before arrival
WSP	1	Trajectory wind speed ($m sec^{-1}$) during the last hour before arrival

1316

1317 Table 1 Aerosol, atmospheric, and ocean parameters utilized in the present study.

1318 DMSPt = Total dimethylsulfoniopropionate in surface ocean waters. TR = temporal

1319 resolution in which the respective data were available. All parameter explanations

1320 starting with "Trajectory" refer to parameters calculated by HYSPLIT4 at each

1321 trajectory step.

1322

1323
1324
1325
1326
1327
1328
1329
1330

Approach	Acronym	Criteria and thresholds	Total number of events	Number of unique events	% of total number of data hours
Percentiles	PCT	N25 >93%-percentile	4143	240	1
Diameter-growth	DGR	D50-Growth >1.5	1199	235	3
Multi-size growth	MEV	Multi-growth >1.6	1191	266	4
Sum			6533	741	

1331
1332
1333
1334
1335

Table 2 Total and unique number of events of new particle formation identified by the three approaches to identify NPF-events, and percent of all data hours covered by unique events.

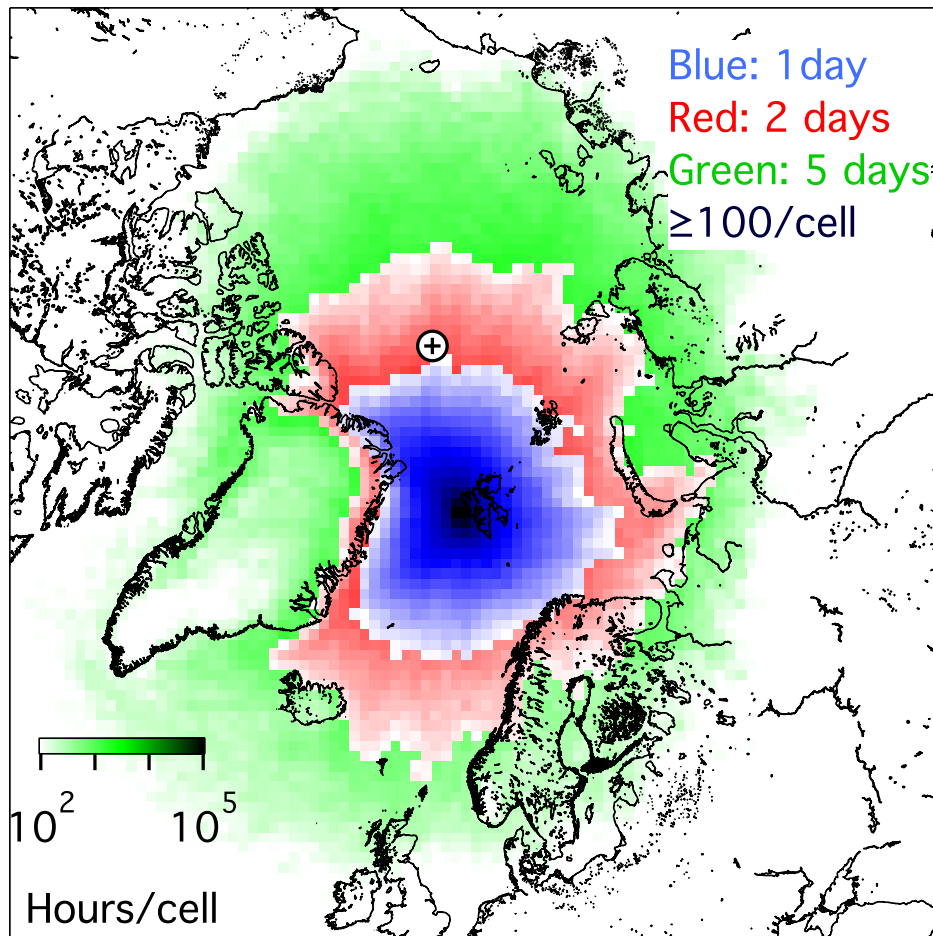
1336

Statistics	J11	GR11	J22	GR22
Minimum	0.1	-1.2	0.1	-0.1
25%	0.4	0.1	0.2	1.0
50%	0.7	0.4	0.3	1.4
75%	1.4	0.6	0.7	1.8
Maximum	19	2.2	22	4

1337

1338 Table 3 Statistics of particle formation rates of DGR-events J11, and J22, ($\text{cm}^{-3}\text{s}^{-1}$), at the
1339 nominal geometric mean diameters 11 nm, and 22 nm and corresponding diameter
1340 growth rates GR11, and GR22, (nmh^{-1}) in the two diameter ranges 5 – 25 nm, and
1341 10 – 50 nm.

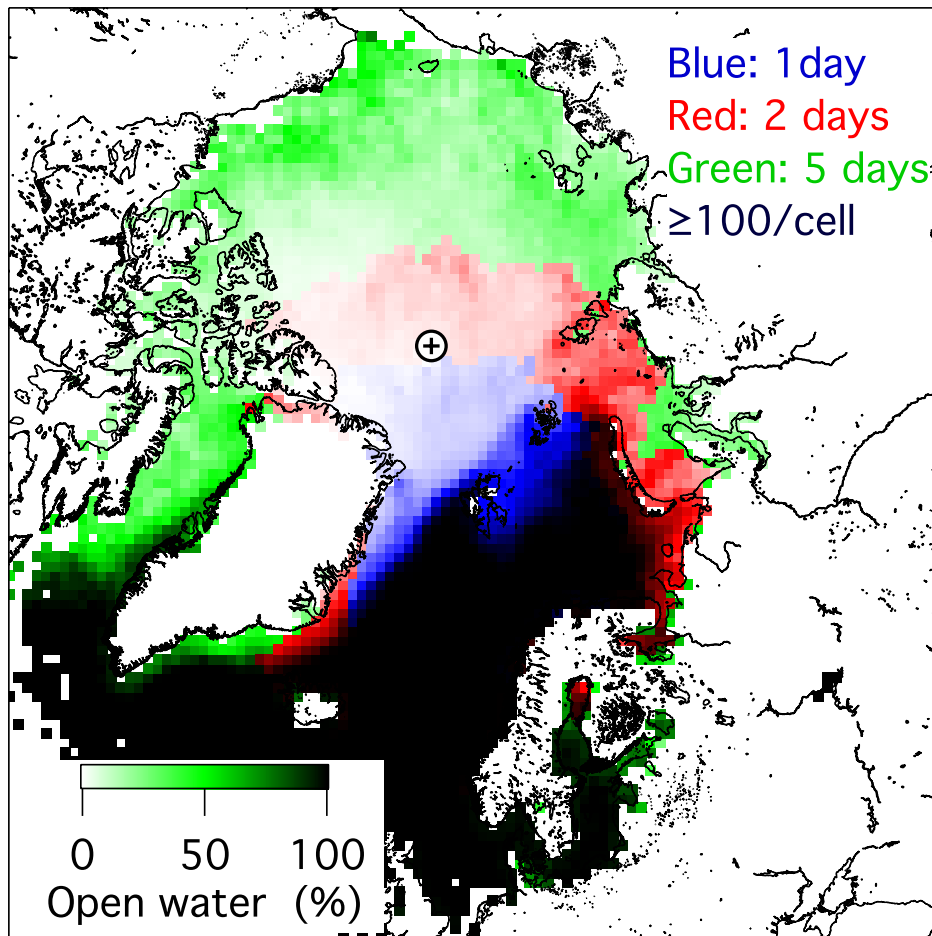
1342



1343

1344 Fig. 1 Map of the regional distribution of 5-day (green), 2-day (red), and 1-day (blue)
 1345 hourly back trajectories to Mt. Zeppelin during the months March through October
 1346 of the years 2006 - 2015. Black symbol: North Pole. The colored areas are covered
 1347 with at least 100 trajectory hours per geocell and the color saturation corresponds to
 1348 the number of trajectory hours per grid cell on a log-scale.

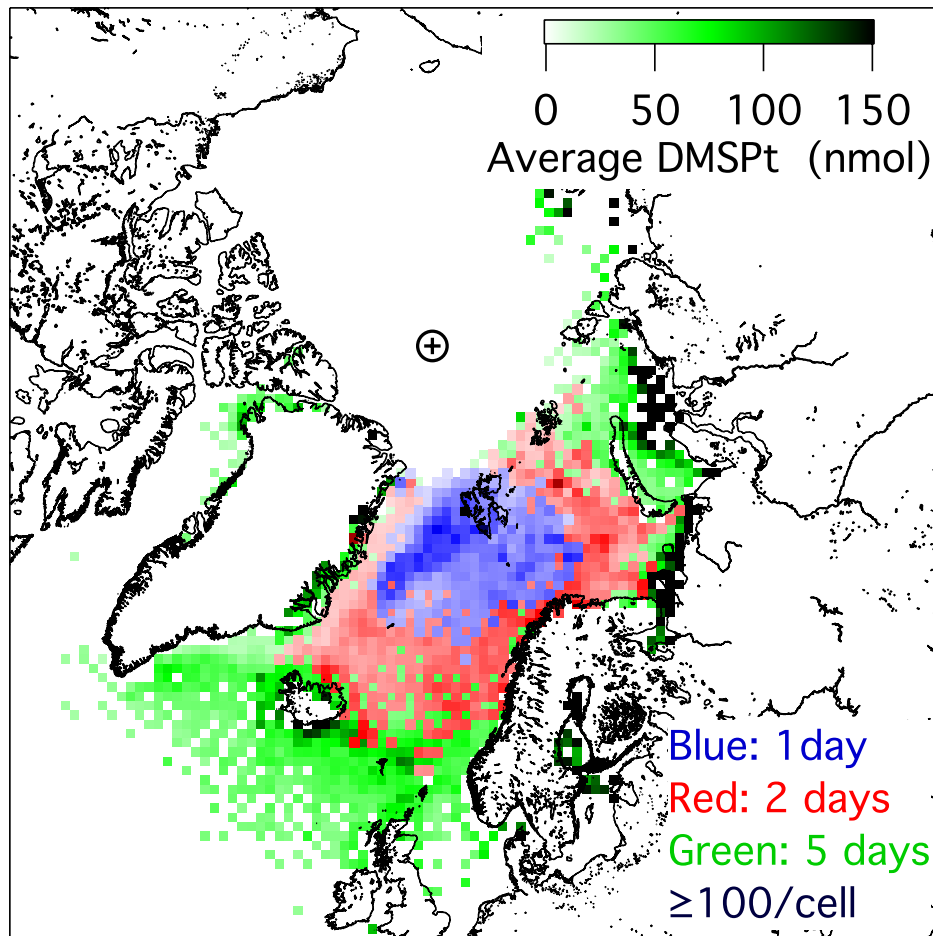
1349



1350

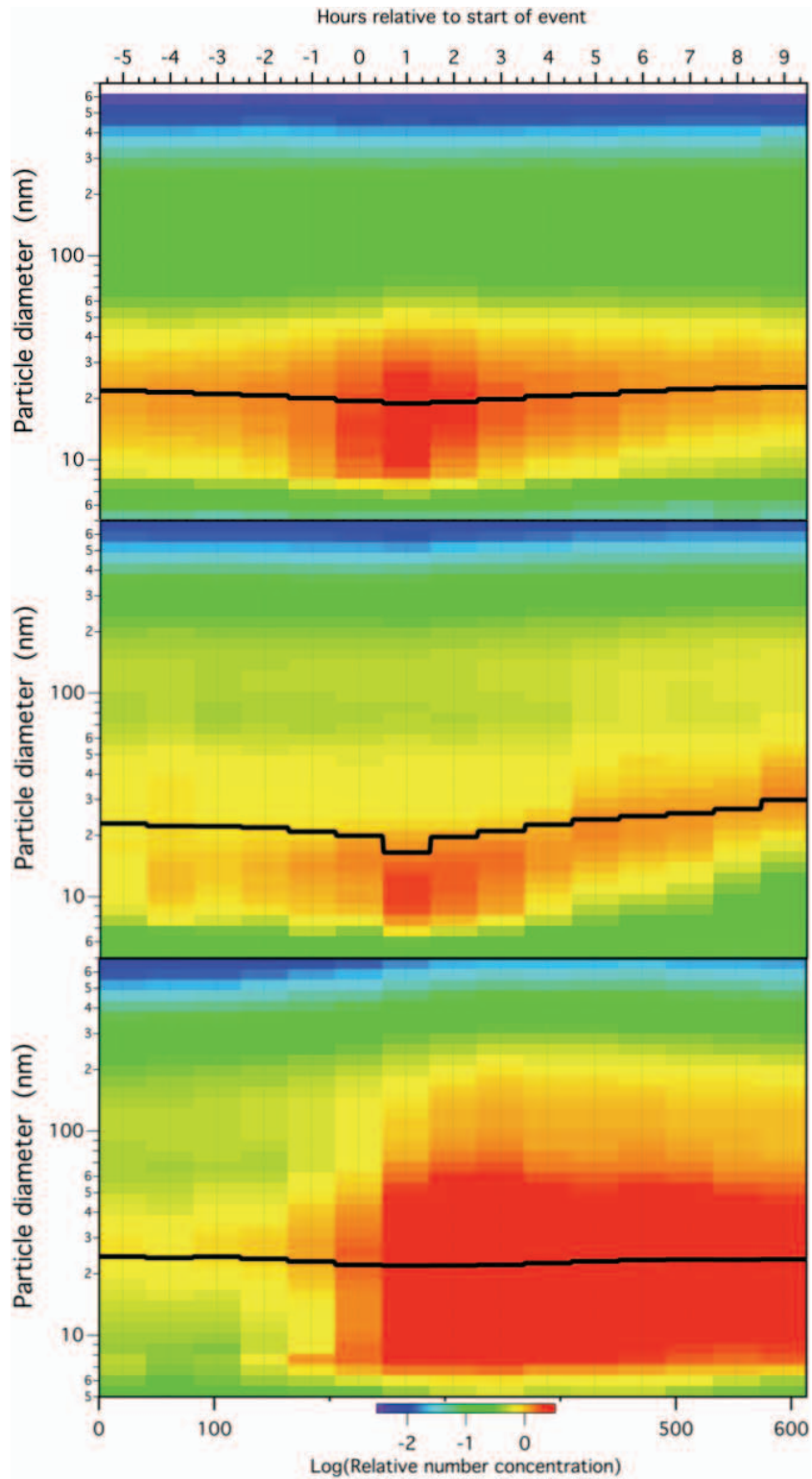
1351 Fig. 2 Map of the regional distribution of open water under 87648 5-day (green), 2-day
 1352 (red), and 1-day (blue) hourly back trajectories to Mt. Zeppelin during the during the
 1353 months March through October of the years 2006-2015. Black symbol: North Pole.
 1354 The areas are covered with at least 100 trajectory hours concurrent with data values
 1355 per geocell.

1356



1357
 1358
 1359
 1360
 1361
 1362
 1363

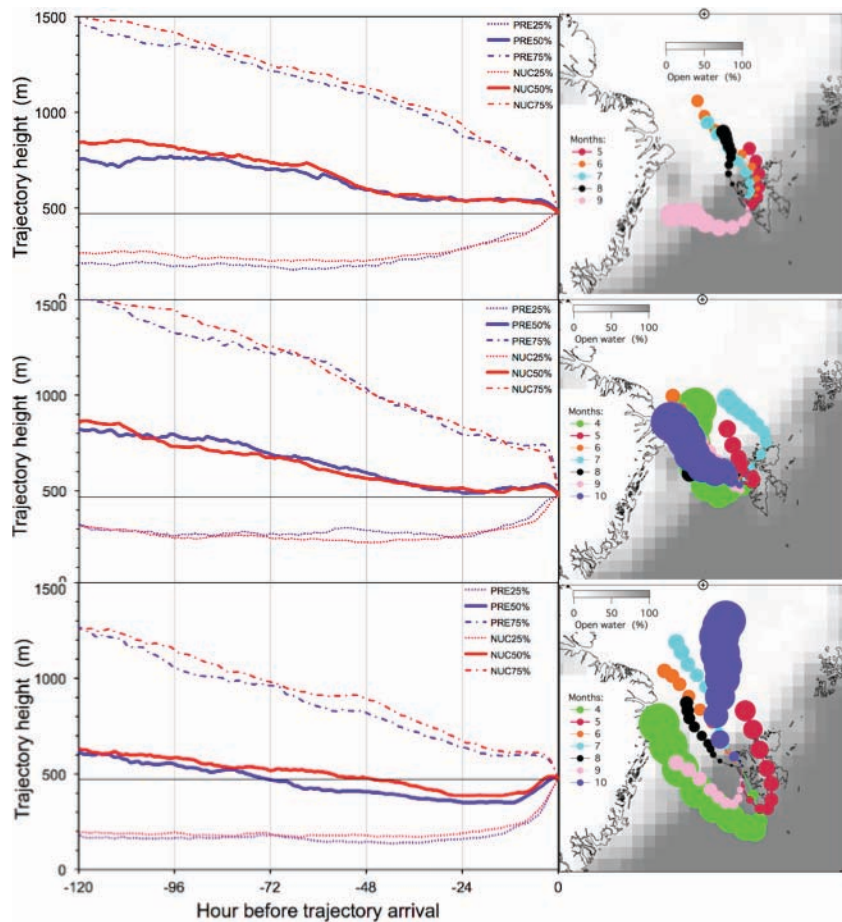
Fig. 3 Map of the regional distribution of DMSPt along 87648 5-day (green), 2-day (red), and 1-day (blue) hourly back trajectories to Mt. Zeppelin during the during the months March through October of the years 2006-2015. Black symbol: North Pole. The relative color scale holds for all colors. The areas are covered with at least 100 trajectory hours with data values per geocell.



1364

1365 Fig.4 Average temporal development of the relative number size distribution before and
 1366 during NPF-events identified by the three approaches. The black curve gives the
 1367 median sub-50-nm particle diameter D50 during the events. Top: PCT-events;
 1368 center: DGR-events; bottom: MEV-events.

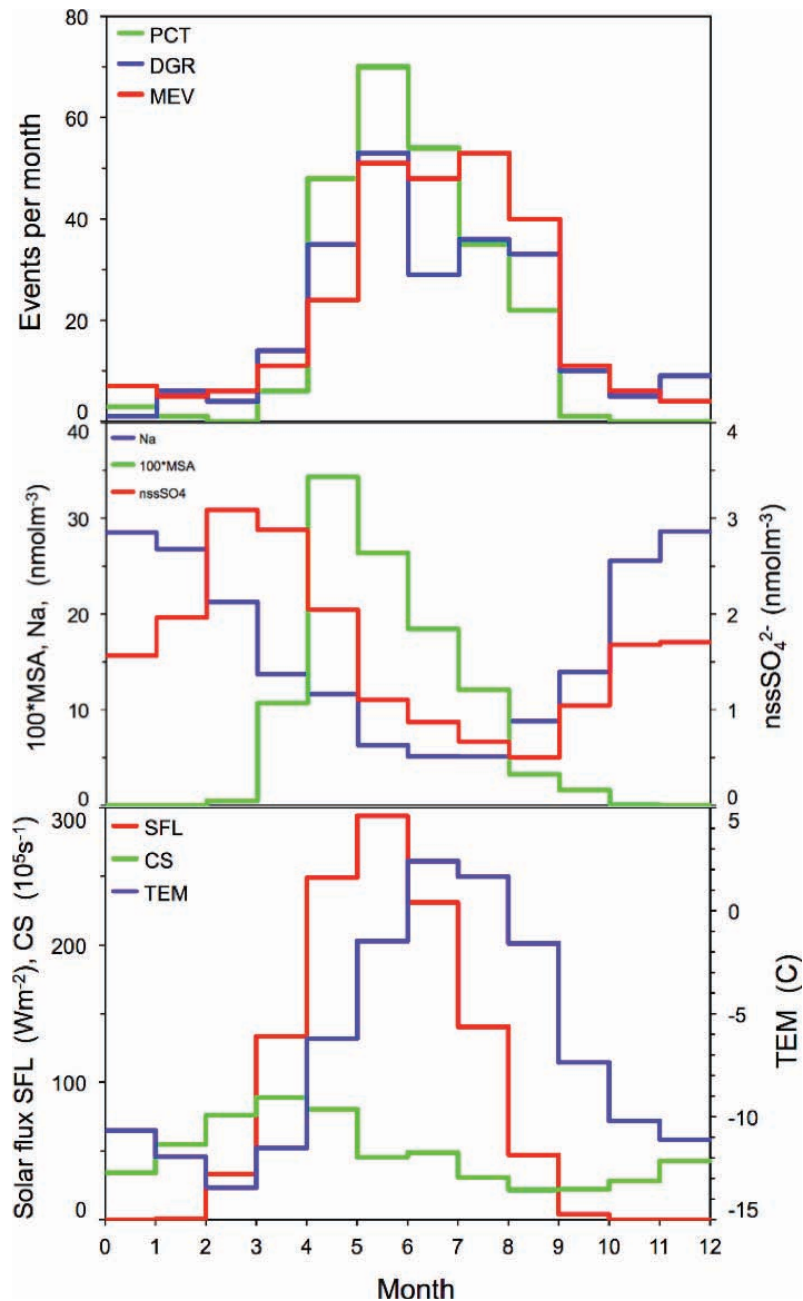
1369



1370
 1371
 1372
 1373
 1374
 1375
 1376
 1377
 1378
 1379
 1380

Fig. 5 Left panels: Median back trajectory height profiles (m) during the six pre-event hours (full line in blue, PRENUC) and during the nine DGR-event hours (full line in red, NUC). 25% and 75% percentiles are shown as dotted, and dash-dotted lines, respectively. Top: PCT-events; center: DGR-events; bottom: MEV-events. The thin horizontal line marks the station level.

Right panels: Average monthly trajectory positions in 12 h steps for the months April through October. Only months with at least 10 NPF-events are shown. The circles comprise 95% of all trajectories at any trajectory step. The underlying grey-scale map indicates July ice cover averaged over the years 2006 – 2015



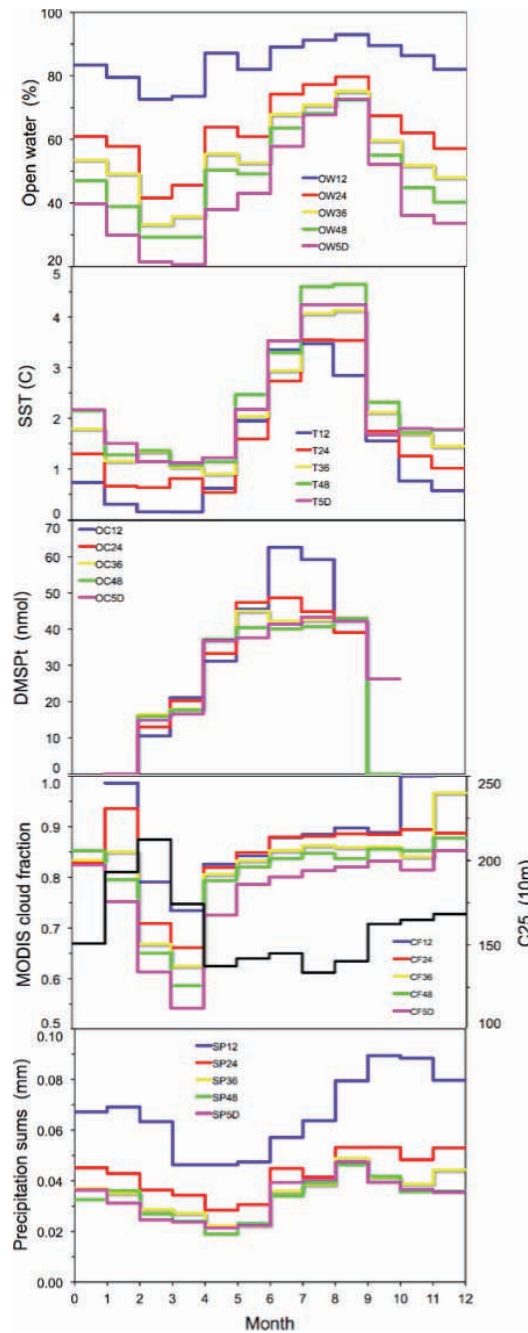
1381

1382 Fig. 6 Top: Monthly numbers of new particle formation events according to the three
 1383 approaches, summed up over the whole period of ten years. PCT: Upper percentile
 1384 of N25; DGR: Diameter growth; MEV: Multiple size events.

1385 Center: Average seasonal distribution of particle composition in nmolm^{-3} .
 1386 Na = sodium, nssSO₄²⁻ = nssSO₄²⁻, MSA = Methane sulfonate times 100.

1387 Bottom: Monthly average solar flux (SFL, red, Wm^{-2}), and temperature (TEM, blue
 1388 °C), and condensation sink, (CS, 10^5s^{-1}), at Mt. Zeppelin, Spitsbergen.

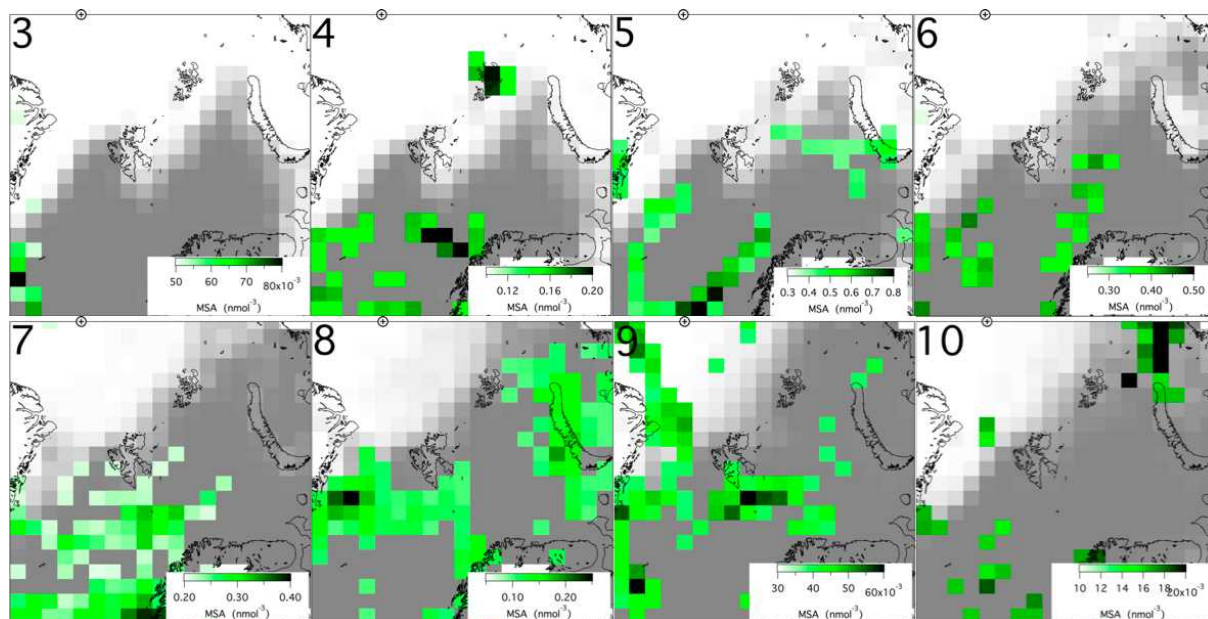
1389



1391

1392 Fig. 7 Monthly averages of environmental parameters averaged along back trajectories to
 1393 Mt. Zeppelin. From top to bottom: OW12-5D: Open water in % during last 12, 24,
 1394 36, and 48h, and days 3-5 before trajectory arrival at Mt. Zeppelin. T12-5D: Same
 1395 for sea surface temperature in °C. OC12-5D: Same for DMSPT in nmol in surface
 1396 waters. CF12-5D: Same for MODIS cloud fraction. SP12-5D: Same for
 1397 precipitation sums in mm. C25 = 25%-percentile of cloud base in decameter.

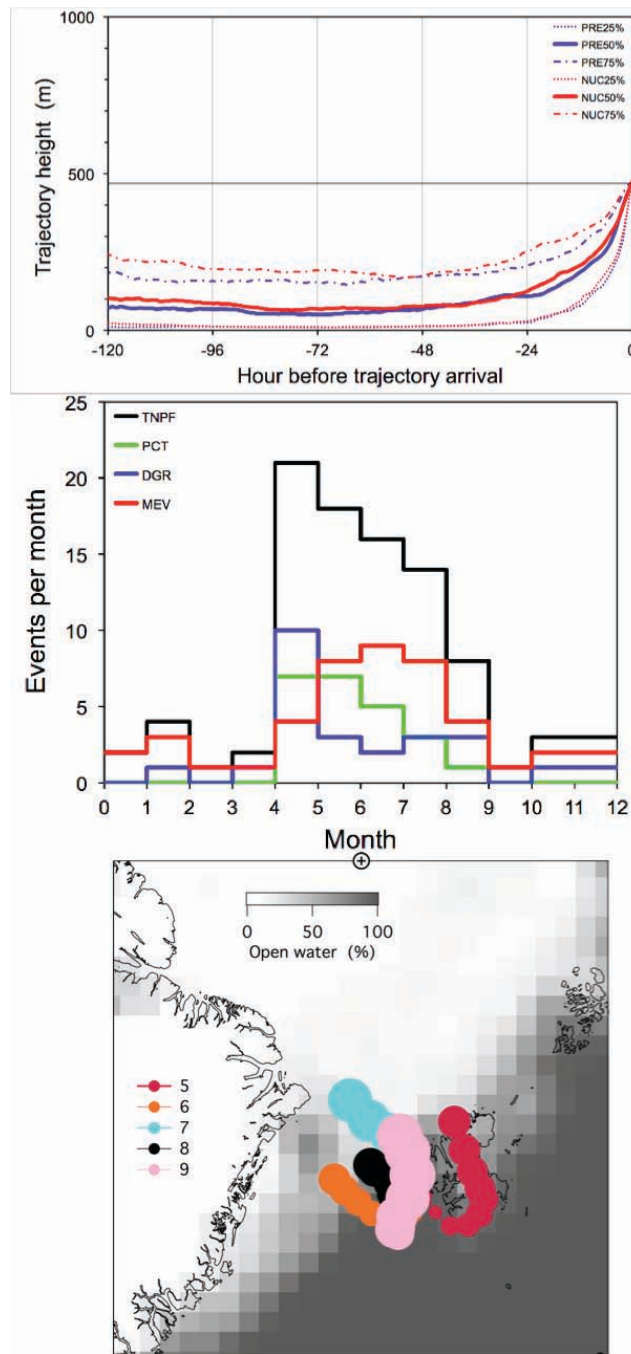
1398



1399

1400 Fig. 8 Average monthly distribution of methane sulfonic acid, (MSA, nmol m^{-3}), during the
 1401 months March – October of the years 2006 – 2015, constructed from MSA-
 1402 concentrations measured on Mt. Zeppelin, which were extrapolated along 5-day back
 1403 trajectories. Average open water percentages during the respective months are
 1404 indicated as white (0% open water) to dark grey (100% open water) areas. The
 1405 position of the North Pole is marked as cross in circle on the upper border of the
 1406 maps.

1407

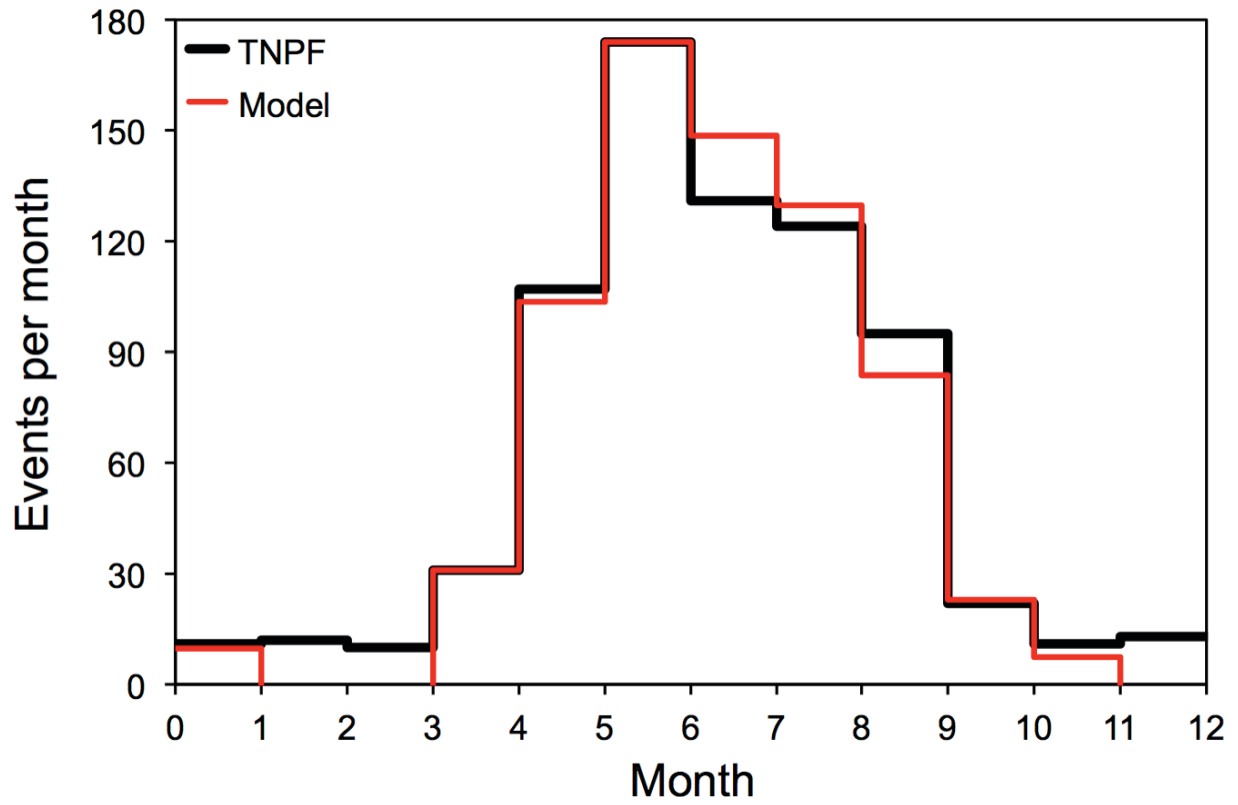


1408

1409 Fig. 9 Characteristics of the subpopulation of 93 NPF-events with back trajectories that
 1410 stayed below 500 m for five days before arrival. Top: Statistics of related vertical
 1411 trajectory coordinates as in Fig. 5. Center: Average monthly occurrence of PCT,
 1412 DGR, and MEV-events, summed up over the whole period of ten years. Bottom:
 1413 Related average monthly trajectory positions in 12 h steps for the months May
 1414 through September. The circles comprise 95% of all trajectories at any trajectory

1415 step. The underlying grey-scale map indicates July ice cover averaged over 2006 –
1416 2015.

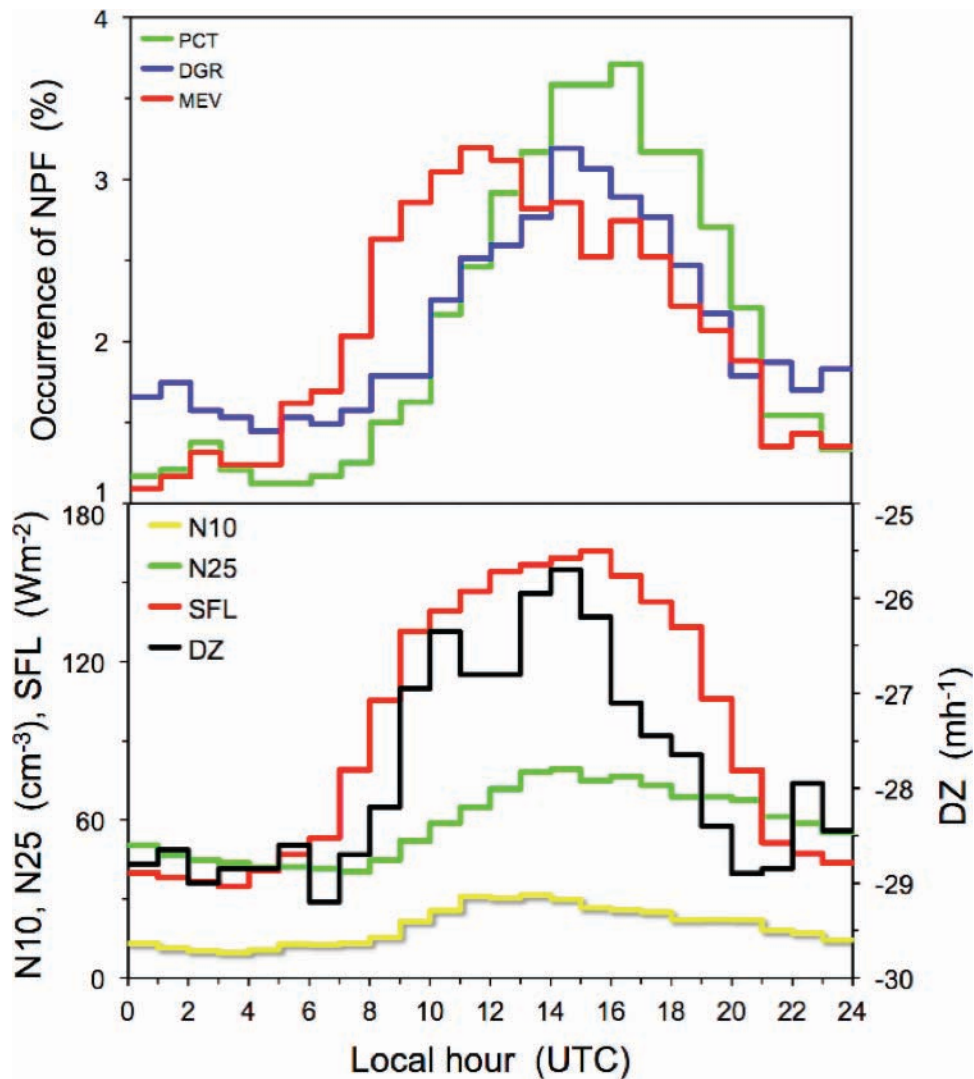
1417



1418

1419 Fig. 10 Average monthly sums of NPF-events due to the three types of new particle
 1420 formation, (TNPF, black), summed up over the whole period of ten years. Red:
 1421 Three-parameter model to describe TNPF.

1422



1423

1424 Fig. 11 Top: Relative average diurnal occurrence of the three types NPF-events. PCT:
 1425 Upper percentile of N25; DGR: Diameter growth; MEV: Multiple size events.
 1426 Bottom: Average diurnal variation of the HYSPLIT-modeled solar flux (SFL, Wm⁻²),
 1427 the integral particle concentrations N10, and N25 in cm⁻³, and of the vertical
 1428 displacement parameter (DZ, mh⁻¹). N10 is based on data of the years 2011 – 2015
 1429 whereas the other parameters are based on data of the years 2006 – 2015.